

A Survey on Occupancy Perception for Autonomous Driving: The Information Fusion Perspective

Huaiyuan Xu^a, Junliang Chen^a, Shiyu Meng^a, Yi Wang^a, Lap-Pui Chau^a

^aDepartment of Electrical and Electronic Engineering, The Hong Kong Polytechnic University, Hong Kong SAR

Abstract

3D occupancy perception technology aims to observe and understand dense 3D environments for autonomous vehicles. Owing to its comprehensive perception capability, this technology is emerging as a trend in autonomous driving perception systems, and is attracting significant attention from both industry and academia. Similar to traditional bird's-eye view (BEV) perception, 3D occupancy perception has the nature of multi-source input and the necessity for information fusion. However, the difference is that it captures vertical structures that are ignored by 2D BEV. In this survey, we review the most recent works on 3D occupancy perception, and provide in-depth analyses of methodologies with various input modalities. Specifically, we summarize general network pipelines, highlight information fusion techniques, and discuss effective network training. We evaluate and analyze the occupancy perception performance of the state-of-the-art on the most popular datasets. Furthermore, challenges and future research directions are discussed. We hope this report will inspire the community and encourage more research work on 3D occupancy perception. A comprehensive list of studies in this survey is available in an active repository that continuously collects the latest work: <https://github.com/HuaiyuanXu/3D-Occupancy-Perception>.

Keywords: Autonomous Driving, Information Fusion, Occupancy Perception.

1. Introduction

1.1. Occupancy Perception in Autonomous Driving

Autonomous driving can improve urban traffic efficiency and reduce energy consumption. For reliable and safe autonomous driving, a crucial capability is to accurately and comprehensively understand the surrounding environment, that is, to perceive the observed world. At present, bird's-eye view (BEV) perception is the mainstream perception pattern [1, 2], with the advantages of absolute scale and no occlusion for describing environments. BEV perception provides a unified representation space for multi-source information fusion (*e.g.*, information from diverse viewpoints, modalities, sensors, and time series) and numerous downstream applications (*e.g.*, explainable decision making and motion planning). However, BEV perception does not monitor height information, thereby cannot provide a complete representation for the 3D scene.

To address this, occupancy perception was proposed for autonomous driving to capture the dense 3D structure of the real world. This burgeoning perception technology aims to infer the occupied state of each voxel for the voxelized world, characterized by a strong generalization capability to open-set objects, irregular-shaped vehicles, and special road structures [3, 4]. Compared with 2D views such as perspective view and bird's-eye view, occupancy perception has a nature of 3D attributes, making it more suitable for 3D downstream tasks, such as 3D detection [5, 6] and segmentation [4].

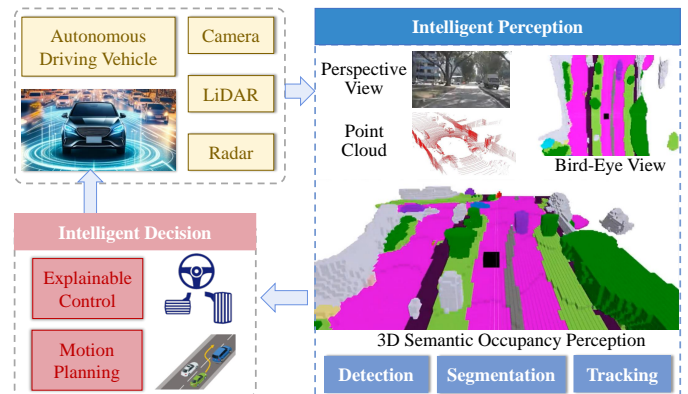


Figure 1: **Autonomous driving vehicle system.** The sensing data from cameras, LiDAR, and radar enable the vehicle to intelligently perceive its surroundings. Subsequently, the intelligent decision module generates control and planning of driving behavior. Occupancy perception surpasses the perception based on the perspective view, bird's-eye view, or point-cloud space, in terms of 3D understanding, density, and no occlusion.

In academia and industry, occupancy perception for holistic 3D scene understanding poses a meaningful impact. On the academic consideration, it is challenging to estimate dense voxel-wise occupancy of the real 3D world from complex input formats, encompassing multiple sensors, modalities, and temporal sequences. Moreover, it is valuable to further reason about semantic categories [7], textual descriptions [8], and motion states [9] for occupied voxels, which paves the way toward a more comprehensive understanding of the environment. From the industrial perspective, the deployment of a LiDAR

¹Lap-Pui Chau is the corresponding author.

Kit on each autonomous vehicle is expensive. With cameras as a cheap alternative to LiDAR, vision-centric occupancy perception is indeed a cost-effective solution that reduces the manufacturing cost for vehicle equipment manufacturers.

1.2. Motivation to Information Fusion Research

The gist of occupancy perception lies in comprehending complete and dense 3D scenes, including understanding occluded areas. However, the observation from a single sensor, such as a 2D image or a point cloud, only captures parts of the scene. Figure 1 intuitively illustrates that an image or a point cloud cannot provide a 3D panorama or a dense environmental scan, resulting in inferior scene perception. To this end, studying information fusion from multiple sensors [10, 11, 12] and multiple frames [4, 7] will facilitate the comprehensive occupancy perception. This is because, on the one hand, information fusion expands the range of spatial perception, and on the other hand, it densifies scene observation. Besides, for occluded regions, integrating multi-frame observations is beneficial, as the same scene is observed by a host of viewpoints, offering sufficient scene features for occlusion inference.

Furthermore, in dynamic outdoor scenarios, where autonomous vehicles must navigate complex environments under varying lighting and weather conditions, the need for stable occupancy perception is paramount. The robustness of perception is crucial for ensuring driving safety and efficiency. At this point, research on multi-modal fusion will promote robust occupancy perception, by combining the strengths of different modalities of data [10, 11, 13, 14]. For example, LiDAR and radar data are insensitive to illumination changes and can sense the precise depth of the scene. This capability is particularly important during nighttime driving or in scenarios where shadows and glare could obscure critical information. Camera data excel in capturing detailed visual texture, being adept at identifying long-distance and color-based environmental elements, such as road signs, traffic lights, and lane markings. The fusion of data from these diverse modalities will present a holistic view of the environment meanwhile against adverse environmental changes.

1.3. Contributions

On related perception topics, 3D semantic segmentation [15, 16] and 3D object detection [17, 18, 19] have been extensively reviewed. However, these tasks do not facilitate a dense understanding of the environment. BEV perception, which addresses this issue, has also been thoroughly reviewed [2, 1]. Our survey focuses on 3D occupancy perception, which captures the environmental height information overlooked by BEV perception. Roldao *et al.* [20] conducted a literature review on 3D scene completion for indoor and outdoor scenes, which is closely related to our focus. Unlike their work, our survey is specifically tailored to autonomous driving scenarios. Moreover, given the multi-source nature of 3D occupancy perception, we provide an in-depth analysis of information fusion techniques for this field. The primary contributions of this survey are three-fold:

- We systematically review the latest research on 3D occupancy perception in the field of autonomous driving, covering the overall research background, comprehensive analyses of its importance, and in-depth discussions on related techniques.
- We provide the taxonomy of 3D occupancy perception, and elaborate on core methodological issues, including network pipelines, multi-source information fusion, and effective network training.
- We present evaluations for 3D occupancy perception, and offer detailed performance comparisons. Furthermore, current limitations and future research directions are discussed.

The remainder of this paper is structured as follows. Sec. 2 provides a brief background on the history, definitions, and related research domains. Sec. 3 details methodological insights. Sec. 4 conducts performance comparisons and analyses. Finally, future research directions are discussed and the survey is concluded in Sec. 5 and 6, respectively.

2. Background

2.1. A Brief History of Occupancy Perception

Occupancy perception is derived from Occupancy Grid Mapping (OGM) [21], which is a classic topic in mobile robot navigation, and aims to generate a grid map from noisy and uncertain measurements. Each grid in this map is assigned a value that scores the probability of the grid space being occupied by obstacles. Semantic occupancy perception originates from SUNCG [22], which predicts the occupied status and semantics of all voxels in an indoor scene from a single image. However, studying occupancy perception in outdoor scenes is imperative for autonomous driving, as opposed to indoor scenes. MonoScene [23] is a pioneering work of outdoor scene occupancy perception using only a monocular camera. Contemporary with MonoScene, Tesla announced its brand-new camera-only occupancy network at the CVPR 2022 workshop on Autonomous Driving [24]. This new network comprehensively understands the 3D environment surrounding a vehicle according to surround-view RGB images. Subsequently, occupancy perception has attracted extensive attention, catalyzing a surge in research on occupancy perception for autonomous driving in recent years.

Early approaches to outdoor occupancy perception primarily used LiDAR input to infer 3D occupancy [25, 26, 27]. However, recent methods have shifted towards more challenging vision-centric 3D occupancy prediction [28, 29, 30, 31]. Presently, a dominant trend in occupancy perception research is vision-centric solutions, complemented by LiDAR-centric methods and multi-modal approaches. Occupancy perception can serve as a unified representation of the 3D physical world within the end-to-end autonomous driving framework [7, 32], followed by downstream applications spanning various driving tasks such as detection, tracking, and planning. The training

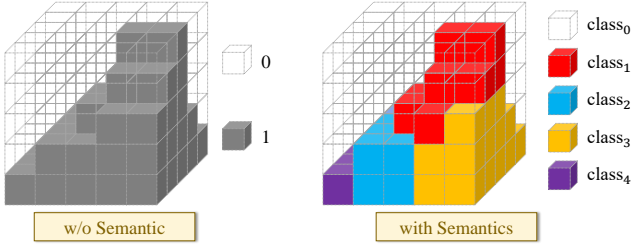


Figure 2: **Illustration of voxel-wise representations with and without semantics.** The left voxel volume depicts the overall occupancy distribution. The right voxel volume incorporates semantic enrichment, where each voxel is associated with a class estimation.

of occupancy perception networks heavily relies on dense 3D occupancy labels, leading to the development of diverse street view occupancy datasets [10, 9, 33, 34]. Recently, taking advantage of the powerful performance of large models, the integration of large models with occupancy perception has shown promise in alleviating the need for cumbersome 3D occupancy labeling [35].

2.2. Task Definition

Occupancy perception aims to extract voxel-wise representations of observed 3D scenes from multi-source inputs. Specifically, this representation involves discretizing a continuous 3D space W into a grid volume V composed of dense voxels. The state of each voxel is described by the value of $\{1, 0\}$ or $\{c_0, \dots, c_n\}$, as illustrated in Fig. 2,

$$W \in \mathbb{R}^3 \rightarrow V \in \{0, 1\}^{X \times Y \times Z} \text{ or } \{c_0, \dots, c_n\}^{X \times Y \times Z}, \quad (1)$$

where 0 and 1 denote the occupied state; c represents semantics; (X, Y, Z) are the length, width, and height of the voxel volume. This voxelized representation offers two primary advantages: (1) it enables the transformation of unstructured data into a voxel volume, thereby facilitating processing by convolution [36] and Transformer [37] architectures; (2) it provides a flexible and scalable representation for 3D scene understanding, striking an optimal trade-off between spatial granularity and memory consumption.

Multi-source input encompasses signals from multiple sensors, modalities, and frames, including common formats such as images and point clouds. We take the multi-camera images $\{I_t^1, \dots, I_t^N\}$ and point cloud P_t of the t -th frame as an input $\Omega_t = \{I_t^1, \dots, I_t^N, P_t\}$. N is the number of cameras. The occupancy perception network Φ_O processes information from the t -th frame and the previous k frames, generating the voxel-wise representation V_t of the t -th frame:

$$V_t = \Phi_O(\Omega_t, \dots, \Omega_{t-k}), \quad \text{s.t. } t - k \geq 0. \quad (2)$$

2.3. Related Works

2.3.1. Bird's-Eye-View Perception

Bird's-eye-view perception represents the 3D scene on a BEV plane. Specifically, it extracts the feature of each entire pillar in 3D space as the feature of the corresponding BEV grid.

This compact representation provides a clear and intuitive depiction of the spatial layout from a top-down perspective. Tesla released its BEV perception-based systematic pipeline [38], which is capable of detecting objects and lane lines in BEV space, for Level 2 highway navigation and smart summoning.

According to the input data, BEV perception is primarily categorized into three groups: BEV camera [39, 40, 41], BEV LiDAR [42, 43], and BEV fusion [44, 45]. Current research predominantly focuses on the BEV camera, the key of which lies in the effective feature conversion from image space to BEV space. To address this challenge, one type of work adopts explicit transformation, which initially estimates the depth for front-view images, then utilizes the camera's intrinsic and extrinsic matrices to map image features into 3D space, and subsequently engages in BEV pooling [40, 45, 46]. Conversely, another type of work employs implicit conversion [41, 47], which implicitly models depth through a cross-attention mechanism and extracts BEV features from image features. Remarkably, the performance of camera-based BEV perception in downstream tasks is now on par with that of LiDAR-based methods [46]. In contrast, occupancy perception can be regarded as an extension of BEV perception. occupancy perception constructs a 3D volumetric space instead of a 2D BEV plane, resulting in a more complete description of the 3D scene.

2.3.2. 3D Semantic Scene completion

3D semantic scene completion (3D SSC) is the task of simultaneously estimating the geometry and semantics of a 3D environment within a given range from limited observations, which requires imagining the complete 3D content of occluded objects and scenes. From a task content perspective, 3D semantic scene completion [23, 34, 48, 49, 50] aligns with semantic occupancy perception [11, 29, 51, 52, 53].

Drawing on prior knowledge, humans excel at estimating the geometry and semantics of 3D environments and occluded regions, but this is more challenging for computers and machines [20]. SSCNet [22] first raised the problem of semantic scene completion and tried to address it via a convolutional neural network. Early 3D SSC research mainly dealt with static indoor scenes [22, 54, 55], such as NYU [56] and SUNCG [22] datasets. After the release of the large-scale outdoor benchmark SemanticKITTI [57], numerous outdoor SSC methods emerged. Among them, MonoScene [23] introduced the first monocular method for outdoor 3D semantic scene completion. It employs 2D-to-3D back projection to lift the 2D image and utilizes consecutive 2D and 3D UNets for semantic scene completion. In recent years, an increasing number of approaches have incorporated multi-camera and temporal information [53, 58, 59] to enhance model comprehension of scenes and reduce completion ambiguity.

2.3.3. 3D Reconstruction from images

3D reconstruction is a traditional but important topic in the computer vision and robotics communities. The objective of 3D reconstruction from images is to construct 3D of an object or scene based on 2D images captured from one or more viewpoints. Early methods exploited shape-from-shading [60]

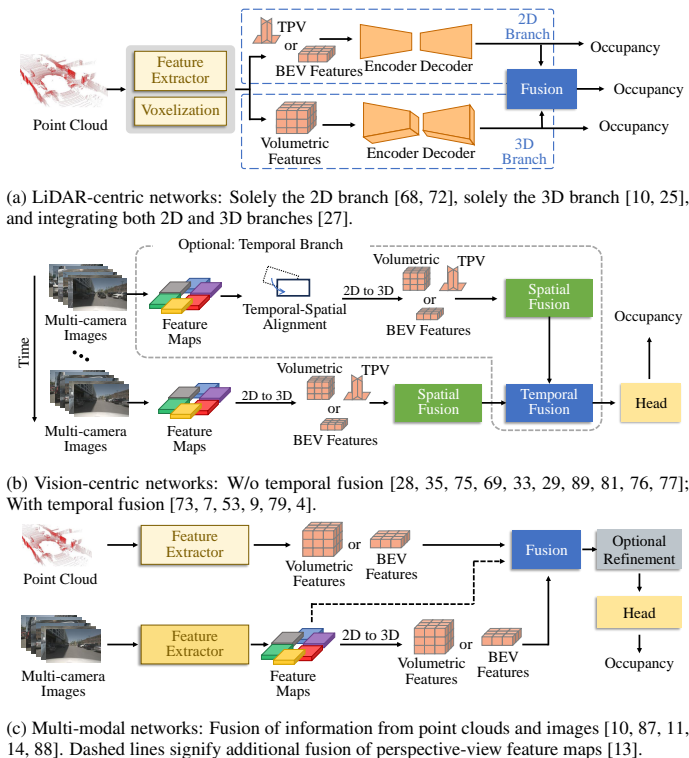


Figure 3: **Architectures for occupancy perception.** For compactness, we do not display all the details but focus on the overall pipelines of LiDAR-centric, vision-centric, and multi-modal occupancy perception approaches.

or structure-from-motion [61]. Afterwards, the neural radiation field (NeRF) [62] introduced a novel paradigm for 3D reconstruction, which learned the density and color fields of 3D scenes, producing results with unprecedented detail and fidelity. However, such performance necessitates substantial training time and resources for rendering [63, 64, 65], especially for high-resolution output. Recently, 3D Gaussian splatting (3D GS) [66] has addressed this issue by redefining a paradigm-shifting approach to scene representation and rendering. Specifically, it represents scene representation with millions of 3D Gaussian functions in an explicit way, achieving faster and more efficient rendering [67]. 3D reconstruction emphasizes the geometric quality and visual appearance of the scene. In comparison, voxel-wise occupancy perception has lower resolution and visual appearance requirements, focusing instead on the occupancy distribution and semantic understanding of the scene.

3. Methodologies

Recent methods of occupancy perception for autonomous driving and their characteristics are detailed in Tab. 1. This table elaborates on the publication venue, input modality, network design, target task, network training and evaluation, and open-source status of each method. Below, we categorize occupancy perception methods into three types, according to the modality of input data. They are LiDAR-centric occupancy perception, vision-centric occupancy perception, and multi-modal

occupancy perception. Subsequently, the training of occupancy networks and their loss functions are discussed. Finally, diverse downstream applications that leverage occupancy perception are presented.

3.1. LiDAR-Centric Occupancy Perception

3.1.1. General Pipeline

LiDAR-centric semantic segmentation [90, 91, 92] only predicts the semantic categories for sparse points. In contrast, LiDAR-centric occupancy perception provides a dense 3D understanding of the environment, crucial to autonomous driving systems. For LiDAR sensing, the acquired point clouds have an inherently sparse nature and suffer from occlusion. This requires that LiDAR-centric occupancy perception not only address the sparse-to-dense occupancy reasoning of the scene, but also achieve the partial-to-complete estimation of objects [11].

Fig. 3a illustrates the general pipeline of LiDAR-centric occupancy perception. The input point cloud first undergoes feature extraction and voxelization, followed by representation enhancement via an encoder-decoder module. Ultimately, the complete and dense occupancy of the scene is inferred. Specifically, given a point cloud $P \in \mathbb{R}^{N \times 3}$ and obtaining the features $F \in \mathbb{R}^{N \times C}$ of each point, a series of initial voxels are produced. These voxels are distributed in a 3D volume [25, 74, 27], a 2D BEV plane [68, 27], or three 2D tri-perspective view planes [72]. This operation constructs the 3D feature volume or 2D feature map, denoted as $V_{\text{init-3D}} \in \mathbb{R}^{X \times Y \times Z \times D}$ and $V_{\text{init-2D}} \in \mathbb{R}^{X \times Y \times D}$ respectively. N represents the number of points; (X, Y, Z) are the length, width, and height; C and D mean the feature dimensions of points and voxels, respectively. In addition to voxelizing in regular Euclidean space, PointOcc [72] builds tri-perspective 2D feature maps in a cylindrical coordinate system. The cylindrical coordinate system aligns more closely with the spatial distribution of points in the LiDAR point cloud, where points closer to the LiDAR sensor are denser than those at farther distances. Therefore, it is reasonable to use smaller-sized cylindrical voxels for fine-grained modeling in nearby areas. The feature extraction and voxelization of point clouds can be formulated as:

$$V_{\text{init-2D/3D}} = \Psi_V(\Phi_P(P)), \quad (3)$$

where Φ_P is the feature extractor such as extracting neural features [93] or directly counting the geometric features of points within the voxel (*e.g.*, mean, minimum, and maximum heights) [27]; Ψ_V stands for pillar or cubic voxelization. Encoder and decoder can be various modules to enhance features. The final 3D occupancy inference involves applying convolution [25, 27, 71] or MLP [68, 72, 74] on the enhanced features to infer the occupied status $\{1, 0\}$ of each voxel, and even estimate its semantic category:

$$V = f_{\text{Conv/MLP}}(ED(V_{\text{init-2D/3D}})), \quad (4)$$

where ED represents encoder and decoder.

Table 1: 3D occupancy perception methods for autonomous driving.

Method	Venue	Modality	Design Choices					Task	Training		Evaluation Datasets		Open Source		
			Feature Format	Multi-Camera	Multi-Frame	Lightweight Design	Head		Supervision	Loss	SemanticKITTI [57] Occ3D-nuScenes [33]	Others	Code	Weight	
LMSCNet [25]	3DV 2020	L	BEV	-	-	2D Conv	3D Conv	P	Strong	CE	✓	-	-	✓	✓
S3CNet [27]	CoRL 2020	L	BEV+Vol	-	-	Sparse Conv	2D & 3D Conv	P	Strong	CE, PA, BCE	✓	-	-	-	-
DIFs [68]	T-PAMI 2021	L	BEV	-	-	2D Conv	MLP	P	Strong	CE, BCE, SC	✓	-	-	-	-
MonoScene [23]	CVPR 2022	C	Vol	-	-	-	3D Conv	P	Strong	CE, FP, Aff	✓	-	-	✓	✓
TPVFormer [29]	CVPR 2023	C	TPV	✓	-	TPV Rp	MLP	P	Strong	CE, LS	✓	-	-	✓	✓
VoxFormer [30]	CVPR 2023	C	Vol	-	✓	-	MLP	P	Strong	CE, BCE, Aff	✓	-	-	✓	✓
OccFormer [52]	ICCV 2023	C	BEV+Vol	-	-	-	Mask Decoder	P	Strong	BCE, MC	✓	-	-	✓	✓
OccNet [7]	ICCV 2023	C	BEV+Vol	✓	✓	-	MLP	P	Strong	Foc	-	-	OpenOcc [7]	✓	-
SurroundOcc [69]	ICCV 2023	C	Vol	✓	-	-	3D Conv	P	Strong	CE, Aff	✓	-	SurroundOcc [69]	✓	✓
OpenOccupancy [10]	ICCV 2023	C+L	Vol	✓	-	-	3D Conv	P	Strong	CE, LS, Aff	✓	-	OpenOccupancy [10]	✓	✓
NDC-Scene [70]	ICCV 2023	C	Vol	-	-	-	3D Conv	P	Strong	CE, FP, Aff	✓	-	-	✓	✓
Occ3D [33]	NeurIPS 2023	C	Vol	✓	-	-	MLP	P	OP	-	-	✓	Occ3D-Waymo [33]	-	-
POP-3D [8]	NeurIPS 2023	C+T+L	Vol	✓	-	-	MLP	OP	Semi	CE, LS, MA	-	-	POP-3D [8]	✓	✓
OCF [71]	arXiv 2023	L	BEV/Vol	-	✓	-	3D Conv	P&F	Strong	BCE, SI	-	-	OCFBen [71]	✓	-
PointOcc [72]	arXiv 2023	L	TPV	-	-	TPV Rp	MLP	P	Strong	Aff	-	-	OpenOccupancy [10]	✓	✓
FlashOcc [73]	arXiv 2023	C	BEV	✓	✓	2D Conv	2D Conv	P	-	-	-	✓	-	✓	✓
OccNeRF [35]	arXiv 2023	C	Vol	✓	✓	-	3D Conv	P	Self	CE, Pho	-	✓	-	✓	✓
SCSF [74]	AAAI 2024	L	Vol	-	✓	Sparse Conv	MLP	F	Strong	CE	✓	-	-	-	-
Vampire [75]	AAAI 2024	C	Vol	✓	-	-	MLP+T	P	Weak	CE, LS	-	✓	-	✓	✓
FastOcc [76]	ICRA 2024	C	BEV	✓	-	2D Conv	MLP	P	Strong	CE, LS, Foc, BCE, Aff	✓	✓	-	-	-
RenderOcc [77]	ICRA 2024	C	Vol	✓	✓	-	MLP+T	P	Weak	CE, SIL	✓	✓	-	✓	✓
MonoOcc [78]	ICRA 2024	C	Vol	-	✓	-	MLP	P	Strong	CE, Aff	✓	-	-	✓	✓
COTR [79]	CVPR 2024	C	Vol	✓	✓	-	Mask Decoder	P	Strong	CE, MC	-	✓	-	-	-
Cam4DOcc [9]	CVPR 2024	C	Vol	✓	✓	-	3D Conv	F	Strong	CE	-	-	Cam4DOcc [9]	✓	✓
PanoOcc [4]	CVPR 2024	C	Vol	✓	✓	-	MLP, DETR	PS	Strong	Foc, LS	-	✓	nuScenes [80]	✓	✓
SelfOcc [81]	CVPR 2024	C	BEV/TPV	✓	-	-	MLP+T	P	Self	Pho	✓	✓	-	✓	✓
Symphonies [82]	CVPR 2024	C	Vol	-	-	-	3D Conv	P	Strong	CE, Aff	✓	-	SSCBench [34]	✓	✓
HASSC [83]	CVPR 2024	C	Vol	✓	✓	-	MLP	P	Strong	CE, Aff, KD	✓	-	-	-	-
SparseOcc [84]	CVPR 2024	C	Vol	✓	-	Sparse Rp	Mask Decoder	P	Strong	-	✓	-	OpenOccupancy [10]	-	-
MVBTS [85]	CVPR 2024	C	Vol	✓	✓	-	MLP+T	P	Self	Pho, KD	-	-	KITTI-360 [86]	✓	-
BRGScene	IJCAI 2024	C	Vol	✓	-	-	3D Conv	P	Strong	CE, BCE, Aff	✓	-	-	✓	✓
OccFusion [11]	arXiv 2024	C+L/R	BEV+Vol	✓	-	-	MLP	P	Strong	Foc, LS, Aff	-	-	SurroundOcc [69]	-	-
Co-Occ [87]	arXiv 2024	C+L	Vol	✓	-	-	3D Conv	P	Strong	CE, LS, Pho	✓	-	SurroundOcc [69]	-	-
HyDRa [13]	arXiv 2024	C+R	BEV+PV	✓	-	-	3D Conv	P	-	-	-	✓	-	-	-
OccGen [88]	arXiv 2024	C+L	Vol	✓	-	-	3D Conv	P	Strong	CE, LS, Aff	✓	-	OpenOccupancy [10]	-	-

Modality: C - Camera; L - LiDAR; R - Radar.

Feature Format: Vol - Volumetric Feature; BEV - Bird's-Eye View Feature; PV - Perspective View Feature; TPV - Tri-Perspective View Feature.

Lightweight Design: TPV Rp - Tri-Perspective View Representation; Sparse Rp - Sparse Representation.

Head: MLP+T - Multi-Layer Perceptron followed by Thresholding.

Task: P - Prediction; F - Forecasting; OP - Open-Vocabulary Prediction; PS - Panoptic Segmentation.

Loss: [Geometric] BCE - Binary Cross Entropy, SIL - Scale-Invariant Logarithmic, SI - Soft-IoU; [Semantic] CE - Cross Entropy, PA - Position Awareness, FP - Frustum Proportion, LS - Lovasz-Softmax, Foc - Focal; [Semantic and Geometric] Aff - Scene-Class Affinity, MC - Mask Classification; [Consistency] SC - Spatial Consistency, MA - Modality Alignment, Pho - Photometric Consistency; [Distillation] KD - Knowledge Distillation.

3.1.2. Information Fusion in LiDAR-Centric Occupancy

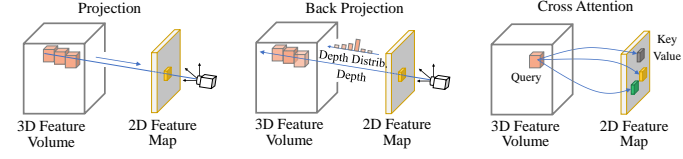
Some works directly utilize a single 2D branch to reason about 3D occupancy, such as DIFs [68] and PointOcc [72]. In these approaches, only 2D feature maps instead of 3D feature volumes are required, resulting in reduced computational demand. However, a significant disadvantage is the partial loss of height information. In contrast, the 3D branch does not compress data in any dimension, thereby protecting the complete 3D scene. To enhance memory efficiency in the 3D branch, LMSCNet [25] turns the height dimension into the feature channel dimension. This adaptation facilitates the use of more efficient 2D convolutions compared to 3D convolutions in the 3D branch. Moreover, integrating information from both 2D and 3D branches can significantly refine occupancy predictions [27].

S3CNet [27] proposes a unique late fusion strategy for integrating information from 2D and 3D branches. This fusion strategy involves a dynamic voxel fusion technique that leverages the results of the 2D branch to enhance the density of the output from the 3D branch. Ablation studies report that this straightforward and direct information fusion strategy can yield a 5-12% performance boost in 3D occupancy perception.

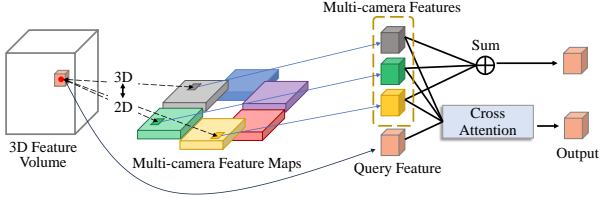
3.2. Vision-Centric Occupancy Perception

3.2.1. General Pipeline

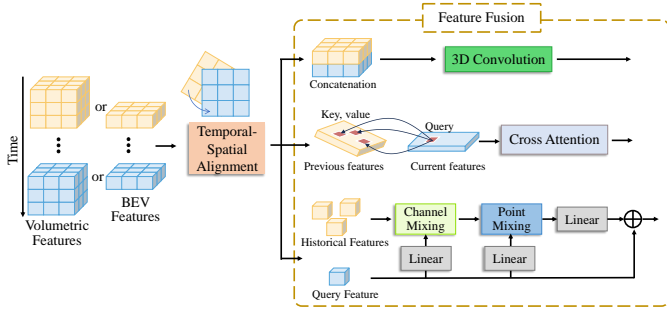
Inspired by Tesla's technology of the perception system for their autonomous vehicles [24], vision-centric occupancy perception has garnered significant attention both in industry and academia. Compared to LiDAR-centric methods, vision-centric occupancy perception, which solely relies on camera



(a) 2D-to-3D transformation. This serves as the fundamental unit for constructing 3D data from 2D observations, typically by projection [28, 23, 50, 35, 85, 94], back projection [52, 73, 75, 76, 84], and cross attention [95, 4, 69, 33, 96].



(b) Spatial information fusion. In areas where multiple cameras have overlapping fields of view, features from these cameras are fused through average [50, 35, 76] or cross attention [95, 4, 29, 69].



(c) Temporal information fusion. Historical and current features undergo the temporal-spatial alignment, and then are fused via convolution [4] (see row 1 in the feature fusion block), cross attention [30, 53, 7] (row 2), and adaptive mixing [96] (row 3).

Figure 4: **Key components of vision-centric 3D occupancy perception.** Specifically, we present techniques for view transformation (*i.e.*, 2D to 3D), multi-camera information integration (*i.e.*, spatial fusion), and historical information integration (*i.e.*, temporal fusion).

sensors, represents a current trend. There are three main reasons: (i) Cameras are cost-effective for large-scale deployment on vehicles. (ii) RGB images capture rich environmental textures, aiding in the understanding of scenes and objects such as traffic signs and lane lines. (iii) The burgeoning advancement of deep learning technologies enables a possibility to achieve 3D occupancy perception from 2D vision. Vision-centric occupancy perception can be divided into monocular solutions [97, 51, 23, 48, 49, 30, 52, 82, 78] and multi-camera solutions [50, 98, 28, 35, 58, 73, 95, 29, 75, 7]. Multi-camera perception, which covers a broader field of view, follows a general pipeline as shown in Fig. 3b. It begins by extracting front-view feature maps from multi-camera images, followed by a 2D-to-3D transformation, spatial information fusion, and optional temporal information fusion, culminating with an occupancy head that infers the environmental 3D occupancy.

Specifically, the 2D feature map $F_{2D}(u, v)$ from the RGB image forms the basis of the vision-centric occupancy pipeline. Its extraction leverages the pre-trained image backbone network Φ_F , such as convolution-based ResNet [36] and Transformer-based ViT [99], $F_{2D}(u, v) = \Phi_F(I(u, v))$. I denotes the input image, (u, v) are pixel coordinates. Since the

front view provides only a 2D perspective, a 2D-to-3D transformation is essential to deduce the depth dimension that the front view lacks, thereby enabling 3D scene perception. The 2D-to-3D transformation is detailed next.

3.2.2. 2D-to-3D Transformation

The transformation is designed to convert front-view features to BEV features [58, 73], TPV features [29], or volumetric features [30, 79, 69] to acquire the missing depth dimension of the front view. Notably, although BEV features are located on the top-view 2D plane, they can encode height information into the channel dimension of the features, thereby representing the 3D scene. The tri-perspective view projects the 3D space into three orthogonal 2D planes, so that each feature in the 3D space can be represented as a combination of three TPV features. The 2D-to-3D transformation is formulated as $F_{BEV/TPV/Vol}(x^*, y^*, z^*) = \Phi_T(F_{2D}(u, v))$, where (x, y, z) represent the coordinates in the 3D space, $*$ means that the specific dimension may not exist in the BEV or TPV planes, Φ_T is the conversion from 2D to 3D. This transformation can be categorized into three types, characterized by using projection [28, 23, 50, 35], back projection [52, 73, 75, 76], and cross attention [95, 4, 69, 33, 96] technologies respectively. Taking the construction of volumetric features as an example, the process is illustrated in Fig. 4a.

(1) *Projection*: It establishes a geometric mapping from the feature volume to the feature map. The mapping is achieved by projecting the voxel centroid in the 3D space onto the 2D front-view feature map through the perspective projection model Ψ_ρ [100], followed by performing sampling Ψ_S by bilinear interpolation [28, 23, 50, 35]. This projection process is formulated as:

$$F_{Vol}(x, y, z) = \Psi_S(F_{2D}(\Psi_\rho(x, y, z, K, RT))), \quad (5)$$

where K and RT are the intrinsics and extrinsics of the camera. However, the problem with the projection-based 2D-to-3D transformation is that along the line of sight, multiple voxels in the 3D space correspond to the same location in the front-view feature map. This leads to many-to-one mapping that introduces the ambiguity in the correspondence between 2D and 3D.

(2) *Back projection*: Back projection is the reverse process of projection. Similarly, it also utilizes perspective projection to establish correspondences between 2D and 3D. However, unlike projection, back projection uses the estimated depth d of each pixel to calculate an accurate one-to-one mapping from 2D to 3D.

$$F_{Vol}(\Psi_V(\Psi_\rho^{-1}(u, v, d, K, RT))) = F_{2D}(u, v), \quad (6)$$

where Ψ_ρ^{-1} indicates the inverse projection function; Ψ_V is voxelization. Since estimating the depth value may introduce errors, it is more effective to predict a discrete depth distribution Dis along the optical ray rather than estimating a specific depth for each pixel [52, 73, 75, 76]. That is, $F_{Vol} = F_{2D} \otimes Dis$, where \otimes denotes outer product. This depth distribution-based

re-projection, derived from LSS [101], has significant advantages. On one hand, it can handle uncertainty and ambiguity in depth perception. For instance, if the depth of a certain pixel is unclear, the model can realize this uncertainty by the depth distribution. On the other hand, this probabilistic method of depth estimation provides greater robustness, particularly in a multi-camera setting. If corresponding pixels in multi-camera images have incorrect depth values to be mapped to the same voxel in the 3D space, their information might be unable to be integrated. In contrast, estimating depth distributions allows for information fusion with depth uncertainty, leading to more robustness and accuracy.

(3) *Cross Attention*: The cross attention-based transformation aims to interact between the feature volume and the feature map in a learnable manner. Consistent with the attention mechanism [37], each volumetric feature in the 3D feature volume acts as the query, and the key and value come from the 2D feature map. However, employing vanilla cross attention for the 2D-to-3D transformation requires considerable computational expense, as each query must attend to all features in the feature map. To optimize for GPU efficiency, many transformation methods [95, 4, 69, 33, 96] adopt deformable cross attention [102], where the query interacts with selected reference features instead of all features in the feature map, therefore greatly reducing computation. Specifically, for each query, we project its 3D position q onto the 2D feature map according to the given intrinsic and extrinsic. We sample some reference features around the projected 2D position p . These sampled features are then weighted and summed according to the deformable attention mechanism:

$$F_{Vol}(q) = \sum_{i=1}^{N_{head}} W_i \sum_{j=1}^{N_{key}} A_{ij} W_{ij} F_{2D}(p + \Delta p_{ij}), \quad (7)$$

where (W_i, W_{ij}) are learnable weights, A_{ij} denotes attention, $p + \Delta p_{ij}$ represents the position of the reference feature, and Δp_{ij} indicates a learnable position shift.

Furthermore, there are some hybrid transformation methods that combine multiple 2D-to-3D transformation techniques. VoxFormer [30] and SGN [48] initially compute a coarse 3D feature volume by per-pixel depth estimation and back projection, and subsequently refine the feature volume using cross attention. COTR [79] has a similar hybrid transformation as VoxFormer and SGN, but it replaces per-pixel depth estimation with estimating depth distributions.

For TPV features, TPVFormer [29] achieves the 2D-to-3D transformation via cross attention. The conversion process differs slightly from that depicted in Fig. 4a, where the 3D feature volume is replaced by a 2D feature map in a specific perspective of three views. For BEV features, the conversion from the front view to the bird’s-eye view can be achieved by cross attention [58] or by back projection and then vertical pooling [58, 73].

3.2.3. Information Fusion in Vision-Centric Occupancy

Sec. 3.2.2 discusses the transformation from a single front-view feature map to a 3D feature volume. In a multi-camera setting, each camera’s front-view feature map describes a part of

the scene. To comprehensively understand the scene, it is necessary to spatially fuse the information from multiple feature maps. Additionally, objects in the scene might be occluded or in motion. Temporally fusing feature maps of multiple frames can help reason about the occluded areas and recognize the motion status of objects.

(1) *Spatial Information Fusion*: The fusion of observations from multiple cameras can create a 3D feature volume with an expanded field of view for scene perception. Within the overlapping area of multi-camera views, a 3D voxel in the feature volume will hit several 2D front-view feature maps after projection. There are two ways to fuse the hit 2D features: average [50, 35, 76] and cross attention [95, 4, 29, 69], as illustrated in Fig. 4b. The averaging operation calculates the mean of multiple features, which simplifies the fusion process and reduces computational costs. However, it assumes the equivalent contribution of different 2D perspectives to perceive the 3D scene. This may not always be the case, especially when certain views are occluded or blurry.

To address this problem, multi-camera cross attention is used to adaptively fuse information from multiple views. Specifically, its process can be regarded as an extension of Eq. 7 by incorporating more camera views. We redefine the deformable attention function as $DA(q, p_i, F_{2D-i})$, where q is a query position in the 3D space, p_i is its projection position on a specific 2D view, and F_{2D-i} is the corresponding 2D front-view feature map. The multi-camera cross attention process can be formulated as:

$$F_{Vol}(q) = \frac{1}{|\nu|} \sum_{i \in \nu} DA(q, p_i, F_{2D-i}), \quad (8)$$

where $F_{Vol}(q)$ represents the feature of the query position in the 3D feature volume, and ν denotes all hit views.

(2) *Temporal Information Fusion*: Recent advancements in vision-based BEV perception systems [103, 41, 104] have demonstrated that integrating temporal information can significantly improve perception performance. Similarly, in vision-based occupancy perception, accuracy and reliability can be improved by combining relevant information from historical features and current perception inputs. The process of temporal information fusion consists of two components: temporal-spatial alignment and feature fusion, as illustrated in Fig. 4c. The temporal-spatial alignment leverages pose information of the ego vehicle to spatially align historical features F_{t-k} with current features. The alignment process is formulated as:

$$F'_{t-k} = \Psi_S(T_{t-k \rightarrow t} \cdot F_{t-k}), \quad (9)$$

where $T_{t-k \rightarrow t}$ is the transformation matrix that converts frame $t-k$ to the current frame t , involving translation and rotation; Ψ_S represents feature sampling.

Once the alignment is completed, the historical and current features are fed to the feature fusion module to enhance the representation, especially to strengthen the reasoning ability for occlusion and the recognition ability of moving objects. There are three main streamlines to feature fusion, namely convolution, cross attention, and adaptive mixing. PanoOcc [4]

concatenates the previous features with the current ones, then fuses them using a set of 3D residual convolution blocks. Many occupancy perception methods [30, 53, 20, 78] utilize cross attention for fusion. The process is similar to multi-camera cross attention (refer to Eq. 8), but the difference is that 3D-space voxels are projected to 2D multi-frame feature maps instead of multi-camera feature maps. Moreover, FullySparse [96] employs adaptive mixing [105] for temporal information fusion. For the query feature of the current frame, FullySparse samples S_n features from historical frames, and aggregates them through adaptive mixing. Specifically, the sampled features are multiplied by the channel mixing matrix W_C and the point mixing matrix W_{S_n} , respectively. These mixing matrices are dynamically generated from the query feature F_q of the current frame:

$$W_{C/S_n} = \text{Linear}(F_q) \in \mathbb{R}^{C \times C} / \mathbb{R}^{S_n \times S_n}. \quad (10)$$

The output of adaptive mixing is flattened, undergoes linear projection, and is then added to the query feature as residuals.

The features resulting from spatial and temporal information fusion are processed by various types of heads to determine 3D occupancy. These include convolutional heads, mask decoder heads, linear projection heads, and linear projection with threshold heads. Convolution-based heads [9, 58, 35, 98, 69, 23] consist of multiple 3D convolutional layers. Mask decoder-based heads [79, 52, 96, 84], inspired by MaskFormer [106] and Mask2Former [107], formalize 3D semantic occupancy prediction into the estimation of a set of binary 3D masks, each associated with a corresponding semantic category. Specifically, they compute per-voxel embeddings and assess per-query embeddings along with their related semantics. The final occupancy predictions are obtained by calculating the dot product of these two embeddings. Linear projection-based heads [4, 29, 33, 48, 78, 30, 83] leverage lightweight MLPs on the dimension of feature channels to produce occupied status and semantics. Furthermore, for the occupancy methods [77, 75, 81, 89, 85] based on NeRF [62], their occupancy heads use two separate MLPs (MLP_σ , MLP_s) to estimate the density volume V_σ and the semantic volume V_S . Then the occupied voxels are selected based on a given confidence threshold τ , and their semantic categories are determined based on V_S :

$$V(x, y, z) = \begin{cases} \text{argmax}(V_S(x, y, z)) & \text{if } V_\sigma(x, y, z) \geq \tau \\ \text{empty} & \text{if } V_\sigma(x, y, z) < \tau, \end{cases} \quad (11)$$

where (x, y, z) represent 3D coordinates.

3.3. Multi-Modal Occupancy Perception

3.3.1. General Pipeline

RGB images captured by cameras provide rich and dense semantic information but are sensitive to weather condition changes and lack precise geometric details. In contrast, point clouds from LiDAR or radar are robust to weather changes and excel at capturing scene geometry with accurate depth measurements. However, they only produce sparse features.

Multi-modal occupancy perception can combine the advantages from multiple modalities, and mitigate the limitations of single-modal perception. Fig. 3c illustrates the general pipeline of multi-modal occupancy perception. Most multi-modal methods [10, 87, 11, 14] map 2D image features into 3D space and then fuse them with point cloud features. Moreover, incorporating 2D perspective-view features in the fusion process can further refine the representation [13]. The fused representation is processed by an optional refinement module and an occupancy head, such as 3D convolution or MLP, to generate the final 3D occupancy predictions. The optional refinement module [88] could be a combination of cross attention, self attention, and diffusion denoising [108].

3.3.2. Information Fusion in Multi-Modal Occupancy

There are three primary multi-modal information fusion techniques to integrate different modality branches: concatenation, summation, and cross attention.

(1) *Concatenation*: Inspired by BEVFusion [45, 44], OccFusion [11] combines 3D feature volumes from different modalities through concatenating them along the feature channel, and subsequently applies convolutional layers. Similarly, RT3DSO [14] concatenates the intensity values of 3D points and their corresponding 2D image features (via projection), and then feeds the combined data to convolutional layers. However, some voxels in 3D space may only contain features from either the point cloud branch or the vision branch. To alleviate this problem, CO-Occ [87] introduces the geometric- and semantic-aware fusion (GSFusion) module, which identifies voxels containing both point-cloud and visual information. This module utilizes a K-nearest neighbors (KNN) search [109] to select the k nearest neighbors of a given position in voxel space within a specific radius. For the i -th non-empty feature FL_i from the point-cloud branch, its nearest visual branch features are represented as $\{FV_{i1}, \dots, FV_{ik}\}$, and a learnable weight ω_i is acquired by linear projection:

$$\omega_i = \text{Linear}(\text{Concat}(FV_{i1}, \dots, FV_{ik})). \quad (12)$$

The resulting LiDAR-vision features are expressed as $FLV = \text{Concat}(FV, FL, FL \cdot \omega)$, where ω denotes the geometric-semantic weight from ω_i .

(2) *Summation*: CONet [10] and OccGen [88] adopt an adaptive fusion module to dynamically integrate the occupancy representations from camera and LiDAR branches. It leverages 3D convolution to process multiple single-modal representations to determine their fusion weight, subsequently applying these weights to sum the LiDAR-branch representation and camera-branch features.

(3) *Cross Attention*: HyDRa [13] proposes the integration of multi-modal information in perspective-view (PV) and BEV representation spaces. Specifically, the PV image features are improved by the BEV point-cloud features using cross attention. Afterwards, the enhanced PV image features are converted into BEV visual representation with estimated depth. These BEV visual features are further enhanced by concatenation with BEV point-cloud features, followed by a simple Squeeze-and-Excitation layer [110]. Finally, the enhanced PV image features

and enhanced BEV visual features are fused through cross attention, resulting in the final occupancy representation.

3.4. Network Training

We classify network training techniques mentioned in the literature based on their supervised training types. The most prevalent type is strongly-supervised learning, while others employ weak, semi, or self supervision for training. This section details these network training techniques and their associated loss functions. The 'Training' column in Tab. 1 offers a concise overview of network training across various occupancy perception methods.

3.4.1. Training with Strong Supervision

Strongly-supervised learning for occupancy perception involves using occupancy labels to train occupancy networks. Most occupancy perception methods adopt this training manner [25, 23, 29, 52, 69, 74, 76, 78, 79, 9, 4, 98]. The corresponding loss functions can be categorized as: geometric losses, which optimize geometric accuracy; semantic losses, which enhance semantic prediction; combined semantic and geometric losses, which encourage both better semantic and geometric accuracy; consistency losses, encouraging overall consistency; and distillation losses, transferring knowledge from the teacher model to the student model. Next, we will provide detailed descriptions.

Among geometric losses, Binary Cross-Entropy (BCE) Loss is the most commonly used [27, 68, 30, 52, 76], which distinguishes empty voxels and occupied voxels. The BCE loss is formulated as:

$$\mathcal{L}_{BCE} = -\frac{1}{N_V} \sum_{i=0}^{N_V} \hat{V}_i \log(V_i) - (1 - \hat{V}_i) \log(1 - V_i), \quad (13)$$

where N_V is the number of voxels in the occupancy volume V . Moreover, there are two other geometric losses: scale-invariant logarithmic loss [111] and soft-IoU loss [112]. SimpleOccupancy [28] calculates the logarithmic difference between the predicted and ground-truth depths as the scale-invariant logarithmic loss. This loss relies on logarithmic rather than absolute differences, therefore offering certain scale invariance. OCF [71] employs the soft-IoU loss to better optimize Intersection over Union (IoU) and prediction confidence.

Cross-entropy (CE) loss is the preferred loss to optimize occupancy semantics [23, 29, 87, 98, 83, 82]. It treats classes as independent entities, and is formally expressed as:

$$\mathcal{L}_{CE} = -\frac{1}{N_C} \sum_{i=0}^{N_V} \sum_{c=0}^{N_C} \omega_c \hat{V}_{ic} \log \left(\frac{e^{V_{ic}}}{\sum_{c'}^{N_C} e^{V_{ic'}}} \right), \quad (14)$$

where (V, \hat{V}) are the ground-truth and predicted semantic occupancy with N_C categories. ω_c is a weight for a specific class c according to the inverse of the class frequency. Moreover, some occupancy perception methods use other semantic losses, which are commonly utilized in semantic segmentation tasks, such as Lovasz-Softmax loss [113] and Focal loss [114]. Furthermore, there are two specialized semantic losses: frustum

proportion loss [23], which provides cues to alleviate occlusion ambiguities from the perspective of the visual frustum, and position awareness loss [115], which leverages local semantic entropy to encourage sharper semantic and geometric gradients.

The losses that can simultaneously optimize semantics and geometry for occupancy perception include scene-class affinity loss [23] and mask classification loss [106, 107]. The former optimizes the combination of precision, recall, and specificity from both geometric and semantic perspectives. The latter is typically associated with a mask decoder head [52, 79]. Mask classification loss, originating from MaskFormer [106] and Mask2Former [107], combines cross-entropy classification loss and a binary mask loss for each predicted mask segment.

The consistency loss and distillation loss correspond to spatial consistency loss [68] and Kullback–Leibler (KL) divergence loss [116], respectively. Spatial consistency loss minimizes the Jensen-Shannon divergence of semantic inference between a given point and some support points in space, thereby enhancing the spatial consistency of semantics. KL divergence, also known as relative entropy, quantifies how one probability distribution deviates from a reference distribution. HASSC [83] adopts KL divergence loss to encourage student models to learn more accurate occupancy from online soft labels provided by the teacher model.

3.4.2. Training with Other Supervisions

(1) *Weak Supervision*: It indicates that occupancy labels are not used, and supervision is derived from alternative labels. For example, point clouds with semantic labels can guide occupancy prediction. Specifically, Vampire [75] and RenderOcc [77] construct density and semantic volumes, which facilitate the inference of semantic occupancy of the scene and the computation of depth and semantic maps through volumetric rendering. These methods do not employ occupancy labels. Alternatively, they project LiDAR point clouds with semantic labels onto the camera plane to acquire ground-truth depth and semantics, which then supervise network training. Since both strongly-supervised and weakly-supervised learning predict geometric and semantic occupancy, the losses used in strongly-supervised learning, such as cross-entropy loss, Lovasz-Softmax loss, and scale-invariant logarithmic loss, are also applicable to weakly-supervised learning.

(2) *Semi Supervision*: It utilizes occupancy labels but does not cover the complete scene, therefore providing only semi supervision for occupancy network training. POP-3D [8] initially generates occupancy labels by processing LiDAR point clouds, where a voxel is recorded as occupied if it contains at least one LiDAR point, and empty otherwise. Given the sparsity and occlusions inherent in LiDAR point clouds, the occupancy labels produced in this manner do not encompass the entire space, meaning that only portions of the scene have their occupancy labelled. POP-3D employs cross-entropy loss and Lovasz-Softmax loss to supervise network training. Moreover, to establish the cross-modal correspondence between text and 3D occupancy, POP-3D proposes to calculate the L2 mean square error between language-image features and 3D-language features as the modality alignment loss.

Table 2: **Overview of 3D occupancy datasets with multi-modal sensors.** Ann.: Annotation. Occ.: Occupancy. C: Camera. L: Lidar. R: Radar. D: Depth map. Flow: 3D occupancy flow. Datasets highlighted in light gray are meta datasets.

Dataset	Year	Meta Dataset	Sensor Data					Annotation		
			Modalities	Scenes	Frames/Clips with Ann.	3D Scans	Images	w/ 3D Occ.?	Classes	w/ Flow?
KITTI [122]	<i>CVPR 2012</i>	-	C+L	22	15K Frames	15K	15k	✓	21	✓
SemanticKITTI [57]	<i>ICCV 2019</i>	KITTI [122]	C+L	22	20K Frames	43K	15k	✓	28	✗
nuScenes [80]	<i>CVPR 2019</i>	-	C+L+R	1,000	40K Frames	390K	1.4M	✗	32	✗
Waymo [123]	<i>CVPR 2020</i>	-	C+L	1,150	230K Frames	230K	12M	✗	23	✓
KITTI-360 [86]	<i>TPAMI 2022</i>	-	C+L	11	80K Frames	320K	80K	✗	19	✗
MonoScene-SemanticKITTI [23]	<i>CVPR 2022</i>	SemanticKITTI [57], KITTI [122]	C	-	4.6K Clips	-	-	✓	19	✗
MonoScene-NYUv2 [23]	<i>CVPR 2022</i>	NYUv2 [56]	C+D	-	1.4K Clips	-	-	✓	10	✗
SSCBench-KITTI-360 [34]	<i>arXiv 2023</i>	KITTI-360 [86]	C	9	-	-	-	✓	19	✗
SSCBench-nuScenes [34]	<i>arXiv 2023</i>	nuScenes [80]	C	850	-	-	-	✓	16	✗
SSCBench-Waymo [34]	<i>arXiv 2023</i>	Waymo [123]	C	1,000	-	-	-	✓	14	✗
OCFBench-Lyft [71]	<i>arXiv 2023</i>	Lyft-Level-5 [124]	L	180	22K Frames	-	-	✓	-	✗
OCFBench-Argoverse [71]	<i>arXiv 2023</i>	Argoverse [125]	L	89	13K Frames	-	-	✓	17	✗
OCFBench-ApolloScape [71]	<i>arXiv 2023</i>	ApolloScape [126]	L	52	4K Frames	-	-	✓	25	✗
OCFBench-nuScenes [71]	<i>arXiv 2023</i>	nuScenes [80]	L	-	-	-	-	✓	16	✗
SurroundOcc [69]	<i>ICCV 2023</i>	nuScenes [80]	C	1,000	-	-	-	✓	16	✗
OpenOccupancy [10]	<i>ICCV 2023</i>	nuScenes [80]	C+L	-	34K Frames	-	-	✓	16	✗
OpenOcc [7]	<i>ICCV 2023</i>	nuScenes [80]	C	850	40K Frames	-	-	✓	16	✗
Occ3D-nuScenes [33]	<i>NeurIPS 2024</i>	nuScenes [80]	C	900	1K Clips, 40K Frames	-	-	✓	16	✗
Occ3D-Waymo [33]	<i>NeurIPS 2024</i>	Waymo [123]	C	1,000	1.1K Clips, 200K Frames	-	-	✓	14	✗
Cam4DOcc [9]	<i>CVPR 2024</i>	nuScenes [80] + Lyft-Level5 [124]	C+L	1,030	51K Frames	-	-	✓	2	✓
OpenScene [127]	<i>CVPR 2024 Challenge</i>	nuPlan [128]	C	-	4M Frames	40M	-	✓	-	✓

(3) *Self Supervision*: It trains occupancy perception networks without any labels. To this end, volume rendering [62] provides a self-supervised signal to encourage consistency across different views from temporal and spatial perspectives, by minimizing photometric differences. MVBTS [85] computes the photometric difference between the rendered RGB image and the target RGB image. However, several other methods calculate this difference between the warped image (from the source image) and the target image [28, 35, 81], where the depth needed for the warping process is acquired by volumetric rendering. OccNeRF [35] believes that the reason for not comparing rendered images is that the large scale of outdoor scenes and few view supervision would make volume rendering networks difficult to converge. Mathematically, the photometric consistency loss [117] combines a L1 loss and an optional structured similarity (SSIM) loss [118] to calculate the reconstruction error between the warped image \hat{I} and the target image I :

$$\mathcal{L}_{Pho} = \frac{\alpha}{2} \left(1 - \text{SSIM} \left(I, \hat{I} \right) \right) + (1 - \alpha) \left\| I, \hat{I} \right\|_1, \quad (15)$$

where α is a hyperparameter weight. Furthermore, OccNeRF leverages cross-Entropy loss for semantic optimization in a self-supervised manner. The semantic labels directly come from pre-trained semantic segmentation models, such as a pre-trained open-vocabulary model Grounded-SAM [119, 120, 121].

4. Evaluation

4.1. Datasets and Metrics

4.1.1. Datasets

There are a variety of datasets to evaluate the performance of occupancy prediction approaches, *e.g.*, the widely used KITTI [122], nuScenes [80], and Waymo [123]. However, most of the datasets only contain 2D semantic segmentation annotations, which is not practical for the training or evaluation of

3D occupancy prediction approaches. To support the benchmarks for 3D occupancy perception, many new datasets such as MonoScene [23], Occ3D [33], and OpenScene [127] are developed based on the previous datasets like nuScenes and Waymo.

Traditional Datasets. Before the development of 3D occupancy based algorithms, KITTI [122], SemanticKITTI [57], nuScenes [80], Waymo [123], and KITTI-360 [86] are widely used benchmarks for 2D semantic perception methods. KITTI contains $\sim 15K$ annotated frames from $\sim 15K$ 3D scans across 22 scenes with camera and LiDAR inputs. SemanticKITTI extends KITTI with more annotated frames ($\sim 20K$) from more 3D scans ($\sim 43K$). nuScenes collects more 3D scans ($\sim 390K$) from 1,000 scenes, resulting in more annotated frames ($\sim 40K$) and supports extra radar inputs. Waymo and KITTI-360 are two large datasets with $\sim 230K$ and $\sim 80K$ frames with annotations, respectively, while Waymo contains more scenes (1000 scenes) than KITTI-360 does (only 11 scenes). The above datasets are the widely adopted benchmarks for 2D perception algorithms before the popularity of 3D occupancy perception. These datasets also serve as the meta datasets of benchmarks for 3D occupancy based perception algorithms.

3D Occupancy Datasets. The occupancy network proposed by Tesla has led the trend of 3D occupancy based perception for autonomous driving. However, the lack of a publicly available large dataset containing 3D occupancy annotations brings difficulty to the development of 3D occupancy perception. To deal with this dilemma, many researchers develop 3D occupancy datasets based on meta datasets like nuScenes and Waymo. MonoScene [23] supporting 3D occupancy annotations is created from SemanticKITTI plus KITTI datasets, and NYUv2 [56] datasets. SSCBench [34] is developed based on KITTI-360, nuScenes, and Waymo datasets with camera inputs. OCFBench [71] built on Lyft-Level-5 [124], Argoverse [125], ApolloScape [126], and nuScenes datasets only contain LiDAR inputs. SurroundOcc [69], OpenOccupancy [10],

and OpenOcc [7] are developed on nuScenes dataset. Occ3D [33] contains more annotated frames with 3D occupancy labels ($\sim 40\text{K}$ based on nuScenes and $\sim 200\text{K}$ frames based on Waymo). Cam4DOcc [9] and OpenScene [127] are two new datasets that contain large-scale 3D occupancy and 3D occupancy flow annotations. Cam4DOcc is based on nuScenes plus Lyft-Level-5 datasets, while OpenScene with $\sim 4\text{M}$ frames with annotations is built on a very large dataset nuPlan [128].

4.1.2. Metrics

(1) *Voxel-level Metrics*: Occupancy prediction without semantic consideration is regarded as class-agnostic perception. It focuses solely on understanding spatial geometry, that is, determining whether each voxel in a 3D space is occupied or empty. The common evaluation metric is voxel-level Intersection-over-Union (IOU), expressed as:

$$\text{IoU} = \frac{TP}{TP + FP + FN}, \quad (16)$$

where TP , FP , and FN represent the number of true positives, false positives, and false negatives. A true positive means that an actual occupied voxel is correctly predicted.

Occupancy prediction that simultaneously infers the occupation status and semantic classification of voxels can be regarded as semantic-geometric perception. In this context, the mean Intersection-over-Union (mIoU) is commonly used as the evaluation metric. The mIoU metric calculates the IoU for each semantic class separately and then averages these IoUs across all classes, excluding the 'empty' class:

$$\text{mIoU} = \frac{1}{N_C} \sum_{i=1}^{N_C} \frac{TP_i}{TP_i + FP_i + FN_i}, \quad (17)$$

where TP_i , FP_i , and FN_i are the number of true positives, false positives, and false negatives for a specific semantic category i . N_C denotes the total number of semantic categories.

(2) *Ray-level Metric*: Although voxel-level IoU and mIoU metrics are widely recognized [9, 79, 73, 50, 35, 81, 69, 78], they still have limitations. Due to unbalanced distribution and occlusion of LiDAR sensing, ground-truth voxel labels from accumulated LiDAR point clouds are imperfect, where the areas not scanned by LiDAR are annotated as empty. Moreover, for thin objects, voxel-level metrics are too strict, as a one-voxel deviation would reduce the IoU values of thin objects to zero. To solve these issues, FullySparse [96] imitates LiDAR's ray casting and proposes ray-level mIoU, which evaluates rays to their closest contact surface. This novel mIoU, combined with the mean absolute velocity error (mAVE), is adopted by the occupancy score (OccScore) metric [127]. OccScore overcomes the shortcomings of voxel-level metrics while also evaluating the performance in perceiving object motion in the scene (*i.e.*, occupancy flow).

The formulation of ray-level mIoU is consistent with Eq. 17 in form but differs in application. The ray-level mIoU evaluates each query ray rather than each voxel. A query ray is considered a true positive if (i) its predicted class label matches the

ground-truth class and (ii) the L1 error between the predicted and ground-truth depths is below a given threshold. The mAVE measures the average velocity error for true positive rays among 8 semantic categories. The final OccScore is calculated as:

$$\text{OccScore} = \text{mIoU} \times 0.9 + \max(1 - \text{mAVE}, 0.0) \times 0.1. \quad (18)$$

4.2. Performance

4.2.1. Perception Accuracy

SemanticKITTI [57] is the first dataset with 3D occupancy labels for outdoor driving scenes. Occ3D-nuScenes [33] is the dataset used in the CVPR 2023 3D Occupancy Prediction Challenge [130]. These two datasets are currently the most popular. Therefore, we summarize the performance of various 3D occupancy methods that are trained and tested on these datasets, as reported in Tab. 3 and 4. These tables further organize occupancy methods according to input modalities and supervised learning types, respectively. The best performances are highlighted in bold. Tab. 3 utilizes the IoU and mIoU metrics to evaluate the 3D geometry and 3D semantics occupancy perception capabilities. Tab. 4 adopts mIoU and mIoU* to assess semantic occupancy perception. Unlike mIoU, the mIoU* metric excludes 'others' and 'other flat' classes and is used by the self-supervised OccNeRF [35]. For fairness, we compute mIoU* of other self-supervised occupancy methods. Notably, the OccScore metric is used in the CVPR 2024 Autonomous Grand Challenge [131], but is not universal currently. Thus, we do not summarize the occupancy performance with this metric. Below, we will compare perception accuracy from three aspects: overall comparison, modality comparison, and supervision comparison.

(1) *Overall Comparison*. Tab. 3 shows that (i) the IoU scores of occupancy networks are less than 50%, while the mIoU scores are less than 30%. The IoU scores (indicating geometric perception, *i.e.*, ignoring semantics) substantially surpass the mIoU scores. This is because predicting occupancy for some semantic categories is challenging, such as bicycles, motorcycles, persons, bicyclists, motorcyclists, poles, and traffic signs. Each of these classes has a small proportion (under 0.3%) in the dataset, and their small sizes in shapes make them difficult to observe and detect. Therefore, if the IOU scores of these categories are low, they significantly impact the overall mIoU value. Because the mIoU calculation, which does not account for category frequency, divides the total IoU scores of all categories by the number of categories. (ii) A higher IoU does not guarantee a higher mIoU. One possible explanation is that the semantic perception capacity (reflected in mIoU) and the geometric perception capacity (reflected in IoU) of an occupancy network are distinct and not positively correlated.

From Tab. 4, it is evident that (i) the mIoU scores of occupancy networks are within 50%, higher than the scores on SemanticKITTI. For example, the mIoU of TPVFormer [29] on SemanticKITTI is 11.26%, but it gets 27.83% on Occ3D-nuScenes. Similarly, OccFormer [52] and SurroundOcc [69] have the same situation. We consider this might be due to the more accurate occupancy labels in Occ3D-nuScenes. SemanticKITTI annotates each voxel based on the LiDAR point

Table 3: **3D occupancy prediction comparison (%) on the SemanticKITTI test set [57]**. Mod.: Modality. C: Camera. L: LiDAR. The IoU evaluates the performance in geometric occupancy perception, and the mIoU evaluates semantic occupancy perception.

Method	Mod.	IoU	mIoU	road	sidewalk	parking	other-grnd	building	car	truck	bicycle	motorcycle	other-veh.	vegetation	trunk	terrain	person	bicyclist	motorcyclist	fence	pole	traf-sign
				(15.30%)	(11.13%)	(1.12%)	(0.56%)	(14.1%)	(3.92%)	(0.16%)	(0.03%)	(0.03%)	(0.20%)	(39.3%)	(0.51%)	(9.17%)	(0.07%)	(0.07%)	(0.05%)	(5.90%)	(0.29%)	(0.08%)
S3CNet [27]	L	45.60	29.53	42.00	22.50	17.00	7.90	52.20	31.20	6.70	41.50	45.00	16.10	39.50	34.00	21.20	45.90	35.80	16.00	31.30	31.00	24.30
LMSCNet [25]	L	56.72	17.62	64.80	34.68	29.02	4.62	38.08	30.89	1.47	0.00	0.00	0.81	41.31	19.89	32.05	0.00	0.00	0.00	21.32	15.01	0.84
JS3C-Net [26]	L	56.60	23.75	64.70	39.90	34.90	14.10	39.40	33.30	7.20	14.40	8.80	12.70	43.10	19.60	40.50	8.00	5.10	0.40	30.40	18.90	15.90
DIFs [68]	L	58.90	23.56	69.60	44.50	41.80	12.70	41.30	35.40	4.70	3.60	2.70	4.70	43.80	27.40	40.90	2.40	1.00	0.00	30.50	22.10	18.50
OpenOccupancy [10]	C+L	-	20.42	60.60	36.10	29.00	13.00	38.40	33.80	4.70	3.00	2.20	5.90	41.50	20.50	35.10	0.80	2.30	0.60	26.00	18.70	15.70
Co-Occ [87]	C+L	-	24.44	72.00	43.50	42.50	10.20	35.10	40.00	6.40	4.40	3.30	8.80	41.20	30.80	40.80	1.60	3.30	0.40	32.70	26.60	20.70
MonoScene [23]	C	34.16	11.08	54.70	27.10	24.80	5.70	14.40	18.80	3.30	0.50	0.70	4.40	14.90	2.40	19.50	1.00	1.40	0.40	11.10	3.30	2.10
TPVFormer [29]	C	34.25	11.26	55.10	27.20	27.40	6.50	14.80	19.20	3.70	1.00	0.50	2.30	13.90	2.60	20.40	1.10	2.40	0.30	11.00	2.90	1.50
OccFormer [52]	C	34.53	12.32	55.90	30.30	31.50	6.50	15.70	21.60	1.20	1.50	1.70	3.20	16.80	3.90	21.30	2.20	1.10	0.20	11.90	3.80	3.70
SurroundOcc [69]	C	34.72	11.86	56.90	28.30	30.20	6.80	15.20	20.60	1.40	1.60	1.20	4.40	14.90	3.40	19.30	1.40	2.00	0.10	11.30	3.90	2.40
NDC-Scene [70]	C	36.19	12.58	58.12	28.05	25.31	6.53	14.90	19.13	4.77	1.93	2.07	6.69	17.94	3.49	25.01	3.44	2.77	1.64	12.85	4.43	2.96
RenderOcc [77]	C	-	8.24	43.64	19.10	12.54	0.00	11.59	14.83	2.47	0.42	0.17	1.78	17.61	1.48	20.01	0.94	3.20	0.00	4.71	1.17	0.88
Symphonies [82]	C	42.19	15.04	58.40	29.30	26.90	11.70	24.70	23.60	3.20	3.60	2.60	5.60	24.20	10.00	23.10	3.20	1.90	2.00	16.10	7.70	8.00
HASSC [83]	C	42.87	14.38	55.30	29.60	25.90	11.30	23.10	23.00	9.80	1.90	1.50	4.90	24.80	9.80	26.50	1.40	3.00	0.00	14.30	7.00	7.10
BRGScene [98]	C	43.34	15.36	61.90	31.20	30.70	10.70	24.20	22.80	8.40	3.40	2.40	6.10	23.80	8.40	27.00	2.90	2.20	0.50	16.50	7.00	7.20
VoxFormer [30]	C	44.15	13.35	53.57	26.52	19.69	0.42	19.54	26.54	7.26	1.28	0.56	7.81	26.10	6.10	33.06	1.93	1.97	0.00	7.31	9.15	4.94
MonoOcc [78]	C	-	15.63	59.10	30.90	27.10	9.80	22.90	23.90	7.20	4.50	2.40	7.70	25.00	9.80	26.10	2.80	4.70	0.60	16.90	7.30	8.40

cloud, that is, assigns labels to voxels based on a majority vote over all labelled points inside the voxel. In contrast, Occ3D-nuScenes utilizes a complex label generation process, including voxel densification, occlusion reasoning, and image-guided voxel refinement. This annotation could produce more precise and dense 3D occupancy labels. (ii) COTR [79] has the best mIoU (46.21%) and also achieves the highest scores in IoU across all categories.

(2) *Modality Comparison*. The input data modality significantly influences on 3D occupancy perception accuracy. The 'Mod.' column in Tab. 3 reports the input modality of various occupancy methods. It can be seen that, due to the accurate depth information provided by LiDAR sensing, LiDAR-centric occupancy methods have more precise perception with higher IoU and mIoU scores. For example, S3CNet [27] has the top mIoU (29.53%) and DIFs [68] achieves the highest IoU (58.90%). We observe that the two multi-modal approaches do not outperform S3CNet and DIFs, indicating that they have not fully leveraged the benefits of multi-modal fusion and the richness of input data. There is considerable potential for further improvement in multi-modal occupancy perception. Besides, although vision-centric occupancy perception has advanced rapidly in recent years, as can be seen from Tab. 3, state-of-the-art vision-centric occupancy methods still have a gap with LiDAR-centric methods in terms of IoU and mIoU. We consider that further improving depth estimation for vision-centric methods is necessary.

(3) *Supervision Comparison*. The 'Sup.' column of Tab. 4 outlines supervised learning types used for training occupancy networks. Training with strong supervision, which directly employs 3D occupancy labels, is the most prevalent type. Tab. 4 shows that occupancy networks based on strongly-supervised learning achieve impressive performance. The mIoU scores

of FastOcc [76], FB-Occ [129], PanoOcc [4], and COTR [79] are significantly higher (12.42%-38.24% increased mIoU) than those of weakly-supervised or self-supervised methods. This is because occupancy labels provided by the dataset are carefully annotated with high accuracy, and can impose strong constraints on network training. However, annotating these dense occupancy labels is time-consuming and laborious. It is necessary to explore network training based on weak or self supervision to reduce reliance on occupancy labels. Vampire [75] is the best-performing method based on weakly-supervised learning, achieving a mIoU score of 28.33%. It demonstrates that semantic LiDAR point clouds can supervise the training of 3D occupancy networks. However, the collection and annotation of semantic LiDAR point clouds are expensive. SelfOcc [81] and OccNeRF [35] are two representative occupancy works based on self-supervised learning. They utilize volume rendering and photometric consistency to acquire self-supervised signals, proving that a network can learn 3D occupancy perception without any labels. However, their performance remains limited, with SelfOcc achieving an mIoU of 7.97% and OccNeRF an mIoU* of 10.81%.

4.2.2. Inference Speed

Recent studies on 3D occupancy perception [76, 96] have begun to consider not only perception accuracy, but also its inference speed. According to the data provided by FastOcc [76] and FullySparse [96], we sort out the inference speeds of 3D occupancy methods, and also report their running platforms, input image sizes, backbone architectures, and occupancy accuracy on the Occ3D-nuScenes dataset, as depicted in Tab. 5.

A practical occupancy method should have high accuracy (mIoU) and fast inference speed (FPS). From Tab. 5, FastOcc achieves a high mIoU (40.75%), comparable to the mIoU of

Table 4: **3D semantic occupancy prediction comparison (%) on the validation set of Occ3D-nuScenes [33]**. Sup. represents the supervised learning type. mIoU* is the mean Intersection-over-Union excluding the 'others' and 'other flat' classes.

Method	Sup.	mIoU		others	barrier	bicycle	bus	car	const. veh.	motorcycle	pedestrian	traffic cone	trailer	truck	drive. suf.	other flat	sidewalk	terrain	manmade	vegetation
		mIoU	mIoU*	■	■	■	■	■	■	■	■	■	■	■	■	■	■	■	■	■
SelfOcc (BEV) [81]	Self	6.76	7.66	0.00	0.00	0.00	0.00	9.82	0.00	0.00	0.00	0.00	0.00	6.97	47.03	0.00	18.75	16.58	11.93	3.81
SelfOcc (TPV) [81]	Self	7.97	9.03	0.00	0.00	0.00	0.00	10.03	0.00	0.00	0.00	0.00	0.00	7.11	52.96	0.00	23.59	25.16	11.97	4.61
SimpleOcc [28]	Self	-	7.99	-	0.67	1.18	3.21	7.63	1.02	0.26	1.80	0.26	1.07	2.81	40.44	-	18.30	17.01	13.42	10.84
OccNeRF [35]	Self	-	10.81	-	0.83	0.82	5.13	12.49	3.50	0.23	3.10	1.84	0.52	3.90	52.62	-	20.81	24.75	18.45	13.19
RenderOcc [77]	Weak	23.93	-	5.69	27.56	14.36	19.91	20.56	11.96	12.42	12.14	14.34	20.81	18.94	68.85	33.35	42.01	43.94	17.36	22.61
Vampire [75]	Weak	28.33	-	7.48	32.64	16.15	36.73	41.44	16.59	20.64	16.55	15.09	21.02	28.47	67.96	33.73	41.61	40.76	24.53	20.26
OccFormer [52]	Strong	21.93	-	5.94	30.29	12.32	34.40	39.17	14.44	16.45	17.22	9.27	13.90	26.36	50.99	30.96	34.66	22.73	6.76	6.97
TPVFormer [29]	Strong	27.83	-	7.22	38.90	13.67	40.78	45.90	17.23	19.99	18.85	14.30	26.69	34.17	55.65	35.47	37.55	30.70	19.40	16.78
Occ3D [33]	Strong	28.53	-	8.09	39.33	20.56	38.29	42.24	16.93	24.52	22.72	21.05	22.98	31.11	53.33	33.84	37.98	33.23	20.79	18.0
SurroundOcc [69]	Strong	38.69	-	9.42	43.61	19.57	47.66	53.77	21.26	22.35	24.48	19.36	32.96	39.06	83.15	43.26	52.35	55.35	43.27	38.02
FastOcc [76]	Strong	40.75	-	12.86	46.58	29.93	46.07	54.09	23.74	31.10	30.68	28.52	33.08	39.69	83.33	44.65	53.90	55.46	42.61	36.50
FB-OCC [129]	Strong	42.06	-	14.30	49.71	30.0	46.62	51.54	29.3	29.13	29.35	30.48	34.97	39.36	83.07	47.16	55.62	59.88	44.89	39.58
PanoOcc [4]	Strong	42.13	-	11.67	50.48	29.64	49.44	55.52	23.29	33.26	30.55	30.99	34.43	42.57	83.31	44.23	54.4	56.04	45.94	40.4
COTR [79]	Strong	46.21	-	14.85	53.25	35.19	50.83	57.25	35.36	34.06	33.54	37.14	38.99	44.97	84.46	48.73	57.60	61.08	51.61	46.72

Table 5: **Inference speed analysis of 3D occupancy perception on the Occ3D-nuScenes [33] dataset**. † indicates data from FullySparse [96]. ‡ means data from FastOcc [76]. R-50 represents ResNet50 [36]. TRT denotes acceleration using the TensorRT SDK [132].

Method	GPU	Input Size	Backbone	mIoU(%)	FPS(Hz)
BEVDet† [40]	A100	704×256	R-50	36.10	2.6
BEVFormer† [41]	A100	1600×900	R-101	39.30	3.0
FB-Occ† [129]	A100	704×256	R-50	10.30	10.3
FullySparse [96]	A100	704×256	R-50	30.90	12.5
SurroundOcc‡ [69]	V100	1600×640	R-101	37.18	2.8
FastOcc [76]	V100	1600×640	R-101	40.75	4.5
FastOcc(TRT) [76]	V100	1600×640	R-101	40.75	12.8

BEVFormer. Notably, FastOcc has a higher FPS value on a lower-performance GPU platform than BEVFormer. Furthermore, after being accelerated by TensorRT [132], the inference speed of FastOcc reaches 12.8Hz.

5. Challenges and Opportunities

5.1. Occupancy-based Applications in Autonomous Driving

3D occupancy perception enables a comprehensive understanding of the 3D world and supports various tasks in autonomous driving. Existing occupancy-based applications include segmentation, detection, flow prediction, and planning. (1) Segmentation: Semantic occupancy perception can essentially be regarded as a 3D semantic segmentation task. (2) Detection: OccupancyM3D [5] and SOGDet [133] are two occupancy-based works to implement 3D object detection. OccupancyM3D first learns occupancy to enhance 3D features, which are then used for 3D detection. SOGDet develops two concurrent tasks: semantic occupancy prediction and 3D object detection, training these tasks simultaneously for mutual enhancement. (3) Flow prediction: Cam4DOcc [9] predicts foreground flow in 3D space from the perspective of occupancy,

and achieves an understanding of changes in the surrounding 3D environment. (4) Planning: OccNet [7] quantifies physical 3D scenes into semantic occupancy, and trains a shared occupancy descriptor. This descriptor is fed to various task heads to implement driving tasks. For example, the motion planning head outputs planning trajectories for ego vehicles.

However, existing occupancy-based applications primarily focus on the perception level, and less on the decision-making level. Given that 3D occupancy is more consistent with the 3D physical world than other perception manners (*e.g.*, bird’s-eye view perception and perspective-view perception), we believe that 3D occupancy holds opportunities for broader applications in autonomous driving. At the perception level, it could improve the accuracy of existing trajectory prediction, 3D object tracking, and 3D lane line detection. At the decision-making level, it could help safer driving decisions and provide 3D explainability for driving behaviors.

5.2. Deployment Efficiency

For complex 3D scenes, large amounts of point cloud data or multi-view visual information always need to be processed and analyzed to extract and update occupancy state information. To achieve real-time performance for the autonomous driving application, solutions commonly need to be computationally complete in a limited amount of time and need to have efficient data structures and algorithm designs. In general, deploying deep learning algorithms on target edge devices is not an easy task.

Currently, some real-time efforts on occupancy tasks have been attempted. For instance, Hou *et al.* [76] proposed a solution, FastOcc, to accelerate the prediction inference speed based on the adjustment of the input resolution, view transformation module, and prediction head. Liu *et al.* [96] proposed SparseOcc, a sparse occupancy network without any dense 3-D features, to minimize the computational costs based on the sparse convolution layers and mask-guided sparse sampling.

Tang *et al.* [84] proposed to adopt the sparse latent representation instead of TPV representation and sparse interpolation operation to avoid information loss and reduce computational complexity. However, the above-mentioned approaches are still some way away from real-time deployment for the adoption of autonomous driving systems.

5.3. Robust 3D Occupancy Perception

In dynamic and unpredictable real-world driving environments, the perception robustness is crucial to autonomous vehicle safety. State-of-the-art 3D occupancy models may be vulnerable to out-of-distribution scenes and data, such as changes in lighting and weather, which would introduce visual biases, and input image blurring, which is caused by vehicle movement. Moreover, sensor malfunctions (*e.g.*, loss of frames and camera views) are common. In light of these challenges, studying robust 3D occupancy perception is valuable.

However, research into robust 3D occupancy is limited, primarily due to the scarcity of datasets. Recently, the ICRA 2024 RoboDrive Challenge [134] provides imperfect scenarios for studying robust 3D occupancy perception. We consider that related works in robust BEV perception [135, 136, 137, 138, 44, 45] could inspire the study of robust occupancy perception. M-BEV [136] proposes random masking and reconstructing camera views to enhance robustness under various missing camera cases. GKT [137] employs coarse projection to achieve a robust BEV representation. In most scenarios involving natural damage, multi-modal models [138, 44, 45] outperform single-modal models by the complementary nature of multi-modal input. Besides, in 3D LiDAR perception, Robo3D [139] distills knowledge from a teacher model with complete point clouds to a student model with imperfect input, thereby enhancing the student model’s robustness. Based on these works, approaching to robust 3D occupancy perception could include, but is not limited to, robust data representation, multiple modalities, network architecture, and learning strategies.

5.4. Generalized 3D Occupancy Perception

3D labels are costly, and large-scale 3D annotations for the real world are impractical. The generalization capabilities of existing networks trained on limited 3D-labelled datasets have not been extensively studied. To get rid of dependence on 3D labels, self-supervised learning represents a potential pathway toward generalized 3D occupancy perception. It learns occupancy perception from a broad range of unlabelled images. However, the performance of current self-supervised occupancy perception [81, 35, 85, 28] is poor. On the Occ3D-nuScene dataset (see Tab. 4), the top accuracy of self-supervised methods is inferior to that of strongly-supervised methods by a large margin. Moreover, current self-supervised methods require training and evaluation with more data. Thus, enhancing self-supervised generalized 3D occupancy perception is an important future research direction.

Furthermore, current 3D occupancy perception can only recognize a set of predefined object categories, which limits its

generalizability and practicality. Recent advances in large language models (LLMs) [140, 141, 142, 143] and large visual-language models (LVLMs) [144, 145, 146, 147, 148] demonstrate a promising ability for reasoning and visual understanding. Integrating these pre-trained large models has been proven to enhance generalization for perception [8]. POP-3D [8] leverages a powerful pre-trained visual-language model [148] to train its network, and achieves open-vocabulary 3D occupancy perception. Therefore, we consider that employing LLMs and LVLMs is a challenge and opportunity for achieving generalized 3D occupancy perception.

6. Conclusion

This paper provided a comprehensive survey of 3D occupancy perception in autonomous driving in recent years. We reviewed and discussed in detail the state-of-the-art LiDAR-centric, vision-centric, and multi-modal perception solutions, and highlighted information fusion techniques for this field. To facilitate further research, detailed performance comparisons of existing occupancy methods are provided. Finally, we described some open challenges that could inspire future research directions in the coming years. We hope that this survey can benefit the community, support further development in autonomous driving, and help inexperienced readers navigate the field.

References

- [1] H. Li, C. Sima, J. Dai, W. Wang, L. Lu, H. Wang, J. Zeng, Z. Li, J. Yang, H. Deng, et al., Delving into the devils of bird’s-eye-view perception: A review, evaluation and recipe, *IEEE Transactions on Pattern Analysis and Machine Intelligence* (2023).
- [2] Y. Ma, T. Wang, X. Bai, H. Yang, Y. Hou, Y. Wang, Y. Qiao, R. Yang, D. Manocha, X. Zhu, Vision-centric bev perception: A survey, *arXiv preprint arXiv:2208.02797* (2022).
- [3] Occupancy networks (2023).
URL <https://www.thinkautonomous.ai/blog/occupancy-networks/>
- [4] Y. Wang, Y. Chen, X. Liao, L. Fan, Z. Zhang, Panoocc: Unified occupancy representation for camera-based 3d panoptic segmentation, *arXiv preprint arXiv:2306.10013* (2023).
- [5] L. Peng, J. Xu, H. Cheng, Z. Yang, X. Wu, W. Qian, W. Wang, B. Wu, D. Cai, Learning occupancy for monocular 3d object detection, *arXiv preprint arXiv:2305.15694* (2023).
- [6] Q. Zhou, J. Cao, H. Leng, Y. Yin, Y. Kun, R. Zimmermann, Sogdet: Semantic-occupancy guided multi-view 3d object detection, *arXiv preprint arXiv:2308.13794* (2023).
- [7] W. Tong, C. Sima, T. Wang, L. Chen, S. Wu, H. Deng, Y. Gu, L. Lu, P. Luo, D. Lin, et al., Scene as occupancy, in: *Proceedings of the IEEE/CVF International Conference on Computer Vision*, 2023, pp. 8406–8415.
- [8] A. Vobecky, O. Siméoni, D. Hurych, S. Gidaris, A. Bursuc, P. Pérez, J. Sivic, Pop-3d: Open-vocabulary 3d occupancy prediction from images, *Advances in Neural Information Processing Systems* 36 (2024).
- [9] J. Ma, X. Chen, J. Huang, J. Xu, Z. Luo, J. Xu, W. Gu, R. Ai, H. Wang, Cam4docc: Benchmark for camera-only 4d occupancy forecasting in autonomous driving applications, *arXiv preprint arXiv:2311.17663* (2023).
- [10] X. Wang, Z. Zhu, W. Xu, Y. Zhang, Y. Wei, X. Chi, Y. Ye, D. Du, J. Lu, X. Wang, Openoccupancy: A large scale benchmark for surrounding semantic occupancy perception, in: *Proceedings of the IEEE/CVF International Conference on Computer Vision*, 2023, pp. 17850–17859.
- [11] Z. Ming, J. S. Berrio, M. Shan, S. Worrall, Occfusion: A straightforward and effective multi-sensor fusion framework for 3d occupancy prediction, *arXiv preprint arXiv:2403.01644* (2024).

- [12] R. Song, C. Liang, H. Cao, Z. Yan, W. Zimmer, M. Gross, A. Festag, A. Knoll, Collaborative semantic occupancy prediction with hybrid feature fusion in connected automated vehicles, arXiv preprint arXiv:2402.07635 (2024).
- [13] P. Wolters, J. Gilg, T. Teepe, F. Herzog, A. Laouichi, M. Hofmann, G. Rigoll, Unleashing hydra: Hybrid fusion, depth consistency and radar for unified 3d perception, arXiv preprint arXiv:2403.07746 (2024).
- [14] S. Sze, L. Kunze, Real-time 3d semantic occupancy prediction for autonomous vehicles using memory-efficient sparse convolution, arXiv preprint arXiv:2403.08748 (2024).
- [15] Y. Xie, J. Tian, X. X. Zhu, Linking points with labels in 3d: A review of point cloud semantic segmentation, IEEE Geoscience and Remote Sensing Magazine 8 (4) (2020) 38–59. doi:10.1109/MGRS.2019.2937630.
- [16] J. Zhang, X. Zhao, Z. Chen, Z. Lu, A review of deep learning-based semantic segmentation for point cloud, IEEE Access 7 (2019) 179118–179133. doi:10.1109/ACCESS.2019.2958671.
- [17] X. Ma, W. Ouyang, A. Simonelli, E. Ricci, 3d object detection from images for autonomous driving: a survey, IEEE Transactions on Pattern Analysis and Machine Intelligence (2023).
- [18] J. Mao, S. Shi, X. Wang, H. Li, 3d object detection for autonomous driving: A comprehensive survey, International Journal of Computer Vision 131 (8) (2023) 1909–1963.
- [19] L. Wang, X. Zhang, Z. Song, J. Bi, G. Zhang, H. Wei, L. Tang, L. Yang, J. Li, C. Jia, et al., Multi-modal 3d object detection in autonomous driving: A survey and taxonomy, IEEE Transactions on Intelligent Vehicles (2023).
- [20] L. Roldao, R. De Charette, A. Verroust-Blondet, 3d semantic scene completion: A survey, International Journal of Computer Vision 130 (8) (2022) 1978–2005.
- [21] S. Thrun, Probabilistic robotics, Communications of the ACM 45 (3) (2002) 52–57.
- [22] S. Song, F. Yu, A. Zeng, A. X. Chang, M. Savva, T. Funkhouser, Semantic scene completion from a single depth image, in: Proceedings of the IEEE conference on computer vision and pattern recognition, 2017, pp. 1746–1754.
- [23] A.-Q. Cao, R. De Charette, Monoscene: Monocular 3d semantic scene completion, in: Proceedings of the IEEE/CVF Conference on Computer Vision and Pattern Recognition, 2022, pp. 3991–4001.
- [24] Workshop on autonomous driving at cvpr 2022 (2022). URL <https://cvpr2022.wad.vision/>
- [25] L. Roldao, R. de Charette, A. Verroust-Blondet, Lmscnet: Lightweight multiscale 3d semantic completion, in: 2020 International Conference on 3D Vision (3DV), IEEE, 2020, pp. 111–119.
- [26] X. Yan, J. Gao, J. Li, R. Zhang, Z. Li, R. Huang, S. Cui, Sparse single sweep lidar point cloud segmentation via learning contextual shape priors from scene completion, in: Proceedings of the AAAI Conference on Artificial Intelligence, Vol. 35, 2021, pp. 3101–3109.
- [27] R. Cheng, C. Agia, Y. Ren, X. Li, L. Bingbing, S3cnet: A sparse semantic scene completion network for lidar point clouds, in: Conference on Robot Learning, PMLR, 2021, pp. 2148–2161.
- [28] W. Gan, N. Mo, H. Xu, N. Yokoya, A simple attempt for 3d occupancy estimation in autonomous driving, arXiv preprint arXiv:2303.10076 (2023).
- [29] Y. Huang, W. Zheng, Y. Zhang, J. Zhou, J. Lu, Tri-perspective view for vision-based 3d semantic occupancy prediction, in: Proceedings of the IEEE/CVF conference on computer vision and pattern recognition, 2023, pp. 9223–9232.
- [30] Y. Li, Z. Yu, C. Choy, C. Xiao, J. M. Alvarez, S. Fidler, C. Feng, A. Anandkumar, Voxformer: Sparse voxel transformer for camera-based 3d semantic scene completion, in: Proceedings of the IEEE/CVF conference on computer vision and pattern recognition, 2023, pp. 9087–9098.
- [31] B. Li, Y. Sun, J. Dong, Z. Zhu, J. Liu, X. Jin, W. Zeng, One at a time: Progressive multi-step volumetric probability learning for reliable 3d scene perception (2024). arXiv:2306.12681.
- [32] Y. Hu, J. Yang, L. Chen, K. Li, C. Sima, X. Zhu, S. Chai, S. Du, T. Lin, W. Wang, et al., Planning-oriented autonomous driving, in: Proceedings of the IEEE/CVF Conference on Computer Vision and Pattern Recognition, 2023, pp. 17853–17862.
- [33] X. Tian, T. Jiang, L. Yun, Y. Mao, H. Yang, Y. Wang, Y. Wang, H. Zhao, Occ3d: A large-scale 3d occupancy prediction benchmark for autonomous driving, Advances in Neural Information Processing Systems 36 (2024).
- [34] Y. Li, S. Li, X. Liu, M. Gong, K. Li, N. Chen, Z. Wang, Z. Li, T. Jiang, F. Yu, et al., Ssbench: Monocular 3d semantic scene completion benchmark in street views, arXiv preprint arXiv:2306.09001 2 (2023).
- [35] C. Zhang, J. Yan, Y. Wei, J. Li, L. Liu, Y. Tang, Y. Duan, J. Lu, Occnerf: Self-supervised multi-camera occupancy prediction with neural radiance fields, arXiv preprint arXiv:2312.09243 (2023).
- [36] K. He, X. Zhang, S. Ren, J. Sun, Deep residual learning for image recognition, in: Proceedings of the IEEE conference on computer vision and pattern recognition, 2016, pp. 770–778.
- [37] A. Vaswani, N. Shazeer, N. Parmar, J. Uszkoreit, L. Jones, A. N. Gomez, L. Kaiser, I. Polosukhin, Attention is all you need, Advances in neural information processing systems 30 (2017).
- [38] Tesla ai day (2021). URL <https://www.youtube.com/watch?v=j0z4FweCy4M>
- [39] Y. Zhang, Z. Zhu, W. Zheng, J. Huang, G. Huang, J. Zhou, J. Lu, Beverse: Unified perception and prediction in birds-eye-view for vision-centric autonomous driving, arXiv preprint arXiv:2205.09743 (2022).
- [40] J. Huang, G. Huang, Z. Zhu, Y. Ye, D. Du, Bevdet: High-performance multi-camera 3d object detection in bird-eye-view, arXiv preprint arXiv:2112.11790 (2021).
- [41] Z. Li, W. Wang, H. Li, E. Xie, C. Sima, T. Lu, Y. Qiao, J. Dai, Bevformer: Learning bird’s-eye-view representation from multi-camera images via spatiotemporal transformers, in: European conference on computer vision, Springer, 2022, pp. 1–18.
- [42] B. Yang, W. Luo, R. Urtasun, Pixor: Real-time 3d object detection from point clouds, in: Proceedings of the IEEE conference on Computer Vision and Pattern Recognition, 2018, pp. 7652–7660.
- [43] B. Yang, M. Liang, R. Urtasun, Hdnet: Exploiting hd maps for 3d object detection, in: Conference on Robot Learning, PMLR, 2018, pp. 146–155.
- [44] Z. Liu, H. Tang, A. Amini, X. Yang, H. Mao, D. L. Rus, S. Han, Bevfusion: Multi-task multi-sensor fusion with unified bird’s-eye view representation, in: 2023 IEEE international conference on robotics and automation (ICRA), IEEE, 2023, pp. 2774–2781.
- [45] T. Liang, H. Xie, K. Yu, Z. Xia, Z. Lin, Y. Wang, T. Tang, B. Wang, Z. Tang, Bevfusion: A simple and robust lidar-camera fusion framework, Advances in Neural Information Processing Systems 35 (2022) 10421–10434.
- [46] Y. Li, Z. Ge, G. Yu, J. Yang, Z. Wang, Y. Shi, J. Sun, Z. Li, Bevdepth: Acquisition of reliable depth for multi-view 3d object detection, in: Proceedings of the AAAI Conference on Artificial Intelligence, Vol. 37, 2023, pp. 1477–1485.
- [47] Y. Jiang, L. Zhang, Z. Miao, X. Zhu, J. Gao, W. Hu, Y.-G. Jiang, Polarformer: Multi-camera 3d object detection with polar transformer, in: Proceedings of the AAAI conference on Artificial Intelligence, Vol. 37, 2023, pp. 1042–1050.
- [48] J. Mei, Y. Yang, M. Wang, J. Zhu, X. Zhao, J. Ra, L. Li, Y. Liu, Camera-based 3d semantic scene completion with sparse guidance network, arXiv preprint arXiv:2312.05752 (2023).
- [49] J. Yao, J. Zhang, Depthssc: Depth-spatial alignment and dynamic voxel resolution for monocular 3d semantic scene completion, arXiv preprint arXiv:2311.17084 (2023).
- [50] R. Miao, W. Liu, M. Chen, Z. Gong, W. Xu, C. Hu, S. Zhou, Occdepth: A depth-aware method for 3d semantic scene completion, arXiv preprint arXiv:2302.13540 (2023).
- [51] A. N. Ganesh, Soccdpt: Semi-supervised 3d semantic occupancy from dense prediction transformers trained under memory constraints, arXiv preprint arXiv:2311.11371 (2023).
- [52] Y. Zhang, Z. Zhu, D. Du, Occformer: Dual-path transformer for vision-based 3d semantic occupancy prediction, in: Proceedings of the IEEE/CVF International Conference on Computer Vision, 2023, pp. 9433–9443.
- [53] S. Silva, S. B. Wannigama, R. Ragel, G. Jayatilaka, S2tpvformer: Spatio-temporal tri-perspective view for temporally coherent 3d semantic occupancy prediction, arXiv preprint arXiv:2401.13785 (2024).
- [54] M. Firman, O. Mac Aodha, S. Julier, G. J. Brostow, Structured prediction of unobserved voxels from a single depth image, in: Proceedings of the IEEE Conference on Computer Vision and Pattern Recognition, 2016, pp. 5431–5440.

- [55] A. Chang, A. Dai, T. Funkhouser, M. Halber, M. Niessner, M. Savva, S. Song, A. Zeng, Y. Zhang, Matterport3d: Learning from rgb-d data in indoor environments, arXiv preprint arXiv:1709.06158 (2017).
- [56] N. Silberman, D. Hoiem, P. Kohli, R. Fergus, Indoor segmentation and support inference from rgb-d images, in: Computer Vision–ECCV 2012: 12th European Conference on Computer Vision, Florence, Italy, October 7–13, 2012, Proceedings, Part V 12, Springer, 2012, pp. 746–760.
- [57] J. Behley, M. Garbade, A. Milioto, J. Quenzel, S. Behnke, C. Stachniss, J. Gall, Semantickitti: A dataset for semantic scene understanding of lidar sequences, in: Proceedings of the IEEE/CVF international conference on computer vision, 2019, pp. 9297–9307.
- [58] C. Min, L. Xiao, D. Zhao, Y. Nie, B. Dai, Multi-camera unified pre-training via 3d scene reconstruction, IEEE Robotics and Automation Letters (2024).
- [59] C. Lyu, S. Guo, B. Zhou, H. Xiong, H. Zhou, 3dopformer: 3d occupancy perception from multi-camera images with directional and distance enhancement, IEEE Transactions on Intelligent Vehicles (2023).
- [60] J.-D. Durou, M. Falcone, M. Sagona, Numerical methods for shape-from-shading: A new survey with benchmarks, Computer Vision and Image Understanding 109 (1) (2008) 22–43.
- [61] J. L. Schonberger, J.-M. Frahm, Structure-from-motion revisited, in: Proceedings of the IEEE conference on computer vision and pattern recognition, 2016, pp. 4104–4113.
- [62] B. Mildenhall, P. P. Srinivasan, M. Tancik, J. T. Barron, R. Ramamoorthi, R. Ng, Nerf: Representing scenes as neural radiance fields for view synthesis, Communications of the ACM 65 (1) (2021) 99–106.
- [63] S. J. Garbin, M. Kowalski, M. Johnson, J. Shotton, J. Valentin, Fast-nerf: High-fidelity neural rendering at 200fps, in: Proceedings of the IEEE/CVF international conference on computer vision, 2021, pp. 14346–14355.
- [64] C. Reiser, S. Peng, Y. Liao, A. Geiger, Kilonerf: Speeding up neural radiance fields with thousands of tiny mlps, in: Proceedings of the IEEE/CVF international conference on computer vision, 2021, pp. 14335–14345.
- [65] T. Takikawa, J. Litalien, K. Yin, K. Kreis, C. Loop, D. Nowrouzezahrai, A. Jacobson, M. McGuire, S. Fidler, Neural geometric level of detail: Real-time rendering with implicit 3d shapes, in: Proceedings of the IEEE/CVF Conference on Computer Vision and Pattern Recognition, 2021, pp. 11358–11367.
- [66] B. Kerbl, G. Kopanas, T. Leimkühler, G. Drettakis, 3d gaussian splatting for real-time radiance field rendering, ACM Transactions on Graphics 42 (4) (2023) 1–14.
- [67] G. Chen, W. Wang, A survey on 3d gaussian splatting, arXiv preprint arXiv:2401.03890 (2024).
- [68] C. B. Rist, D. Emmerichs, M.ENZWEILER, D. M. Gavrilu, Semantic scene completion using local deep implicit functions on lidar data, IEEE transactions on pattern analysis and machine intelligence 44 (10) (2021) 7205–7218.
- [69] Y. Wei, L. Zhao, W. Zheng, Z. Zhu, J. Zhou, J. Lu, Surroundocc: Multi-camera 3d occupancy prediction for autonomous driving, in: Proceedings of the IEEE/CVF International Conference on Computer Vision, 2023, pp. 21729–21740.
- [70] J. Yao, C. Li, K. Sun, Y. Cai, H. Li, W. Ouyang, H. Li, Ndc-scene: Boost monocular 3d semantic scene completion in normalized device coordinates space, in: 2023 IEEE/CVF International Conference on Computer Vision (ICCV), IEEE Computer Society, 2023, pp. 9421–9431.
- [71] X. Liu, M. Gong, Q. Fang, H. Xie, Y. Li, H. Zhao, C. Feng, Lidar-based 4d occupancy completion and forecasting, arXiv preprint arXiv:2310.11239 (2023).
- [72] S. Zuo, W. Zheng, Y. Huang, J. Zhou, J. Lu, Pointocc: Cylindrical tri-perspective view for point-based 3d semantic occupancy prediction, arXiv preprint arXiv:2308.16896 (2023).
- [73] Z. Yu, C. Shu, J. Deng, K. Lu, Z. Liu, J. Yu, D. Yang, H. Li, Y. Chen, Flashocc: Fast and memory-efficient occupancy prediction via channel-to-height plugin, arXiv preprint arXiv:2311.12058 (2023).
- [74] Z. Wang, Z. Ye, H. Wu, J. Chen, L. Yi, Semantic complete scene forecasting from a 4d dynamic point cloud sequence, in: Proceedings of the AAAI Conference on Artificial Intelligence, Vol. 38, 2024, pp. 5867–5875.
- [75] J. Xu, L. Peng, H. Cheng, L. Xia, Q. Zhou, D. Deng, W. Qian, W. Wang, D. Cai, Regulating intermediate 3d features for vision-centric autonomous driving, in: Proceedings of the AAAI Conference on Artificial Intelligence, Vol. 38, 2024, pp. 6306–6314.
- [76] J. Hou, X. Li, W. Guan, G. Zhang, D. Feng, Y. Du, X. Xue, J. Pu, Fastocc: Accelerating 3d occupancy prediction by fusing the 2d bird’s-eye view and perspective view, arXiv preprint arXiv:2403.02710 (2024).
- [77] M. Pan, J. Liu, R. Zhang, P. Huang, X. Li, L. Liu, S. Zhang, Renderocc: Vision-centric 3d occupancy prediction with 2d rendering supervision, arXiv preprint arXiv:2309.09502 (2023).
- [78] Y. Zheng, X. Li, P. Li, Y. Zheng, B. Jin, C. Zhong, X. Long, H. Zhao, Q. Zhang, Monoocc: Digging into monocular semantic occupancy prediction, arXiv preprint arXiv:2403.08766 (2024).
- [79] Q. Ma, X. Tan, Y. Qu, L. Ma, Z. Zhang, Y. Xie, Cotr: Compact occupancy transformer for vision-based 3d occupancy prediction, arXiv preprint arXiv:2312.01919 (2023).
- [80] H. Caesar, V. Bankiti, A. H. Lang, S. Vora, V. E. Liong, Q. Xu, A. Krishnan, Y. Pan, G. Baldan, O. Beijbom, nuscenes: A multimodal dataset for autonomous driving, in: Proceedings of the IEEE/CVF conference on computer vision and pattern recognition, 2020, pp. 11621–11631.
- [81] Y. Huang, W. Zheng, B. Zhang, J. Zhou, J. Lu, Selfocc: Self-supervised vision-based 3d occupancy prediction, arXiv preprint arXiv:2311.12754 (2023).
- [82] H. Jiang, T. Cheng, N. Gao, H. Zhang, W. Liu, X. Wang, Symphonize 3d semantic scene completion with contextual instance queries, arXiv preprint arXiv:2306.15670 (2023).
- [83] S. Wang, J. Yu, W. Li, W. Liu, X. Liu, J. Chen, J. Zhu, Not all voxels are equal: Hardness-aware semantic scene completion with self-distillation, arXiv preprint arXiv:2404.11958 (2024).
- [84] P. Tang, Z. Wang, G. Wang, J. Zheng, X. Ren, B. Feng, C. Ma, Sparseocc: Rethinking sparse latent representation for vision-based semantic occupancy prediction, arXiv preprint arXiv:2404.09502 (2024).
- [85] K. Han, D. Muhle, F. Wimbauer, D. Cremers, Boosting self-supervision for single-view scene completion via knowledge distillation, arXiv preprint arXiv:2404.07933 (2024).
- [86] Y. Liao, J. Xie, A. Geiger, Kitti-360: A novel dataset and benchmarks for urban scene understanding in 2d and 3d, IEEE Transactions on Pattern Analysis and Machine Intelligence 45 (3) (2022) 3292–3310.
- [87] J. Pan, Z. Wang, L. Wang, Co-occ: Coupling explicit feature fusion with volume rendering regularization for multi-modal 3d semantic occupancy prediction, arXiv preprint arXiv:2404.04561 (2024).
- [88] G. Wang, Z. Wang, P. Tang, J. Zheng, X. Ren, B. Feng, C. Ma, Occgen: Generative multi-modal 3d occupancy prediction for autonomous driving, arXiv preprint arXiv:2404.15014 (2024).
- [89] S. Boeder, F. Gigengack, B. Risse, Occlownet: Towards self-supervised occupancy estimation via differentiable rendering and occupancy flow, arXiv preprint arXiv:2402.12792 (2024).
- [90] L. Li, H. P. Shum, T. P. Breckon, Less is more: Reducing task and model complexity for 3d point cloud semantic segmentation, in: Proceedings of the IEEE/CVF Conference on Computer Vision and Pattern Recognition, 2023, pp. 9361–9371.
- [91] L. Kong, J. Ren, L. Pan, Z. Liu, Lasermix for semi-supervised lidar semantic segmentation, in: Proceedings of the IEEE/CVF Conference on Computer Vision and Pattern Recognition, 2023, pp. 21705–21715.
- [92] P. Tang, H.-M. Xu, C. Ma, Prototransfer: Cross-modal prototype transfer for point cloud segmentation, in: Proceedings of the IEEE/CVF International Conference on Computer Vision, 2023, pp. 3337–3347.
- [93] C. R. Qi, H. Su, K. Mo, L. J. Guibas, Pointnet: Deep learning on point sets for 3d classification and segmentation, in: Proceedings of the IEEE conference on computer vision and pattern recognition, 2017, pp. 652–660.
- [94] Z. Ming, J. S. Berrio, M. Shan, S. Worrall, Inversematrixvt3d: An efficient projection matrix-based approach for 3d occupancy prediction, arXiv preprint arXiv:2401.12422 (2024).
- [95] Y. Lu, X. Zhu, T. Wang, Y. Ma, Octreeocc: Efficient and multi-granularity occupancy prediction using octree queries, arXiv preprint arXiv:2312.03774 (2023).
- [96] H. Liu, H. Wang, Y. Chen, Z. Yang, J. Zeng, L. Chen, L. Wang, Fully sparse 3d occupancy prediction, arXiv preprint arXiv:2312.17118 (2024).
- [97] Z. Tan, Z. Dong, C. Zhang, W. Zhang, H. Ji, H. Li, Ovo: Open-vocabulary occupancy, arXiv preprint arXiv:2305.16133 (2023).
- [98] B. Li, Y. Sun, Z. Liang, D. Du, Z. Zhang, X. Wang, Y. Wang, X. Jin,

- W. Zeng, Bridging stereo geometry and bev representation with reliable mutual interaction for semantic scene completion (2024).
- [99] A. Dosovitskiy, L. Beyer, A. Kolesnikov, D. Weissenborn, X. Zhai, T. Unterthiner, M. Dehghani, M. Minderer, G. Heigold, S. Gelly, et al., An image is worth 16x16 words: Transformers for image recognition at scale, arXiv preprint arXiv:2010.11929 (2020).
- [100] D. Scaramuzza, F. Fraundorfer, Visual odometry [tutorial], IEEE robotics & automation magazine 18 (4) (2011) 80–92.
- [101] J. Philion, S. Fidler, Lift, splat, shoot: Encoding images from arbitrary camera rigs by implicitly unprojecting to 3d, in: Computer Vision–ECCV 2020: 16th European Conference, Glasgow, UK, August 23–28, 2020, Proceedings, Part XIV 16, Springer, 2020, pp. 194–210.
- [102] Z. Xia, X. Pan, S. Song, L. E. Li, G. Huang, Vision transformer with deformable attention, in: Proceedings of the IEEE/CVF conference on computer vision and pattern recognition, 2022, pp. 4794–4803.
- [103] J. Park, C. Xu, S. Yang, K. Keutzer, K. M. Kitani, M. Tomizuka, W. Zhan, Time will tell: New outlooks and a baseline for temporal multi-view 3d object detection, in: The Eleventh International Conference on Learning Representations, 2022.
- [104] Y. Liu, J. Yan, F. Jia, S. Li, A. Gao, T. Wang, X. Zhang, PetrV2: A unified framework for 3d perception from multi-camera images, in: Proceedings of the IEEE/CVF International Conference on Computer Vision, 2023, pp. 3262–3272.
- [105] H. Liu, Y. Teng, T. Lu, H. Wang, L. Wang, Sparsebev: High-performance sparse 3d object detection from multi-camera videos, in: Proceedings of the IEEE/CVF International Conference on Computer Vision, 2023, pp. 18580–18590.
- [106] B. Cheng, A. G. Schwing, A. Kirillov, Per-pixel classification is not all you need for semantic segmentation, 2021.
- [107] B. Cheng, I. Misra, A. G. Schwing, A. Kirillov, R. Girdhar, Masked-attention mask transformer for universal image segmentation, 2022.
- [108] J. Ho, A. Jain, P. Abbeel, Denoising diffusion probabilistic models, Advances in neural information processing systems 33 (2020) 6840–6851.
- [109] T. Cover, P. Hart, Nearest neighbor pattern classification, IEEE transactions on information theory 13 (1) (1967) 21–27.
- [110] J. Hu, L. Shen, G. Sun, Squeeze-and-excitation networks, in: Proceedings of the IEEE conference on computer vision and pattern recognition, 2018, pp. 7132–7141.
- [111] D. Eigen, C. Puhrsch, R. Fergus, Depth map prediction from a single image using a multi-scale deep network, Advances in neural information processing systems 27 (2014).
- [112] Y. Huang, Z. Tang, D. Chen, K. Su, C. Chen, Batching soft iou for training semantic segmentation networks, IEEE Signal Processing Letters 27 (2019) 66–70.
- [113] M. Berman, A. R. Triki, M. B. Blaschko, The lovász-softmax loss: A tractable surrogate for the optimization of the intersection-over-union measure in neural networks, in: Proceedings of the IEEE conference on computer vision and pattern recognition, 2018, pp. 4413–4421.
- [114] T.-Y. Lin, P. Goyal, R. Girshick, K. He, P. Dollár, Focal loss for dense object detection, in: Proceedings of the IEEE international conference on computer vision, 2017, pp. 2980–2988.
- [115] J. Li, Y. Liu, X. Yuan, C. Zhao, R. Siegwart, I. Reid, C. Cadena, Depth based semantic scene completion with position importance aware loss, IEEE Robotics and Automation Letters 5 (1) (2019) 219–226.
- [116] S. Kullback, R. A. Leibler, On information and sufficiency, The annals of mathematical statistics 22 (1) (1951) 79–86.
- [117] R. Garg, V. K. Bg, G. Carneiro, I. Reid, Unsupervised cnn for single view depth estimation: Geometry to the rescue, in: Computer Vision–ECCV 2016: 14th European Conference, Amsterdam, The Netherlands, October 11–14, 2016, Proceedings, Part VIII 14, Springer, 2016, pp. 740–756.
- [118] Z. Wang, A. C. Bovik, H. R. Sheikh, E. P. Simoncelli, Image quality assessment: from error visibility to structural similarity, IEEE transactions on image processing 13 (4) (2004) 600–612.
- [119] Idea-research/grounded-segment-anything (2023).
URL <https://github.com/IDEA-Research/Grounded-Segment-Anything>
- [120] A. Kirillov, E. Mintun, N. Ravi, H. Mao, C. Rolland, L. Gustafson, T. Xiao, S. Whitehead, A. C. Berg, W.-Y. Lo, et al., Segment anything, in: Proceedings of the IEEE/CVF International Conference on Computer Vision, 2023, pp. 4015–4026.
- [121] S. Liu, Z. Zeng, T. Ren, F. Li, H. Zhang, J. Yang, C. Li, J. Yang, H. Su, J. Zhu, et al., Grounding dino: Marrying dino with grounded pre-training for open-set object detection, arXiv preprint arXiv:2303.05499 (2023).
- [122] A. Geiger, P. Lenz, R. Urtasun, Are we ready for autonomous driving? the kitti vision benchmark suite, in: 2012 IEEE conference on computer vision and pattern recognition, IEEE, 2012, pp. 3354–3361.
- [123] P. Sun, H. Kretzschmar, X. Dotiwalla, A. Chouard, V. Patnaik, P. Tsui, J. Guo, Y. Zhou, Y. Chai, B. Caine, et al., Scalability in perception for autonomous driving: Waymo open dataset, in: Proceedings of the IEEE/CVF conference on computer vision and pattern recognition, 2020, pp. 2446–2454.
- [124] J. Houston, G. Zuidhof, L. Bergamini, Y. Ye, L. Chen, A. Jain, S. Omari, V. Igloukov, P. Ondruska, One thousand and one hours: Self-driving motion prediction dataset, in: Conference on Robot Learning, PMLR, 2021, pp. 409–418.
- [125] M.-F. Chang, J. Lambert, P. Sangkloy, J. Singh, S. Bak, A. Hartnett, D. Wang, P. Carr, S. Lucey, D. Ramanan, et al., Argoverse: 3d tracking and forecasting with rich maps, in: Proceedings of the IEEE/CVF conference on computer vision and pattern recognition, 2019, pp. 8748–8757.
- [126] X. Huang, X. Cheng, Q. Geng, B. Cao, D. Zhou, P. Wang, Y. Lin, R. Yang, The apolloscape dataset for autonomous driving, in: Proceedings of the IEEE conference on computer vision and pattern recognition workshops, 2018, pp. 954–960.
- [127] O. Contributors, Openscene: The largest up-to-date 3d occupancy prediction benchmark in autonomous driving, <https://github.com/OpenDriveLab/OpenScene> (2023).
- [128] H. Caesar, J. Kabzan, K. S. Tan, W. K. Fong, E. Wolff, A. Lang, L. Fletcher, O. Beijbom, S. Omari, nuPlan: A closed-loop ml-based planning benchmark for autonomous vehicles, arXiv preprint arXiv:2106.11810 (2021).
- [129] Z. Li, Z. Yu, D. Austin, M. Fang, S. Lan, J. Kautz, J. M. Alvarez, Fb-occ: 3d occupancy prediction based on forward-backward view transformation, arXiv preprint arXiv:2307.01492 (2023).
- [130] Cvpr 2023 3d occupancy prediction challenge (2023).
URL <https://opendrivelab.com/challenge2023/>
- [131] Cvpr 2024 autonomous grand challenge (2024).
URL https://opendrivelab.com/challenge2024/#occupancy_and_flow
- [132] H. Vanholder, Efficient inference with tensorrt, in: GPU Technology Conference, Vol. 1, 2016.
- [133] Q. Zhou, J. Cao, H. Leng, Y. Yin, Y. Kun, R. Zimmermann, Sogdet: Semantic-occupancy guided multi-view 3d object detection, in: Proceedings of the AAAI Conference on Artificial Intelligence, Vol. 38, 2024, pp. 7668–7676.
- [134] Icaro 2024 robdribe challenge (2024).
URL <https://robodrive-24.github.io/#tracks>
- [135] S. Xie, L. Kong, W. Zhang, J. Ren, L. Pan, K. Chen, Z. Liu, Robobev: Towards robust bird’s eye view perception under corruptions, arXiv preprint arXiv:2304.06719 (2023).
- [136] S. Chen, Y. Ma, Y. Qiao, Y. Wang, M-bev: Masked bev perception for robust autonomous driving, in: Proceedings of the AAAI Conference on Artificial Intelligence, Vol. 38, 2024, pp. 1183–1191.
- [137] S. Chen, T. Cheng, X. Wang, W. Meng, Q. Zhang, W. Liu, Efficient and robust 2d-to-bev representation learning via geometry-guided kernel transformer, arXiv preprint arXiv:2206.04584 (2022).
- [138] Y. Kim, J. Shin, S. Kim, I.-J. Lee, J. W. Choi, D. Kum, Crn: Camera radar net for accurate, robust, efficient 3d perception, in: Proceedings of the IEEE/CVF International Conference on Computer Vision, 2023, pp. 17615–17626.
- [139] L. Kong, Y. Liu, X. Li, R. Chen, W. Zhang, J. Ren, L. Pan, K. Chen, Z. Liu, Robo3d: Towards robust and reliable 3d perception against corruptions, in: Proceedings of the IEEE/CVF International Conference on Computer Vision, 2023, pp. 19994–20006.
- [140] H. W. Chung, L. Hou, S. Longpre, B. Zoph, Y. Tay, W. Fedus, Y. Li, X. Wang, M. Dehghani, S. Brahma, et al., Scaling instruction-finetuned language models, Journal of Machine Learning Research 25 (70) (2024) 1–53.
- [141] L. Zheng, W.-L. Chiang, Y. Sheng, S. Zhuang, Z. Wu, Y. Zhuang, Z. Lin, Z. Li, D. Li, E. Xing, et al., Judging llm-as-a-judge with mt-bench and chatbot arena, Advances in Neural Information Processing Systems 36

- (2024).
- [142] OpenAI, Chatgpt (2021).
URL <https://www.openai.com/>
 - [143] H. Touvron, T. Lavril, G. Izacard, X. Martinet, M.-A. Lachaux, T. Lacroix, B. Rozière, N. Goyal, E. Hambro, F. Azhar, et al., Llama: Open and efficient foundation language models (2023), arXiv preprint arXiv:2302.13971 (2023).
 - [144] D. Zhu, J. Chen, X. Shen, X. Li, M. Elhoseiny, Minigt-4: Enhancing vision-language understanding with advanced large language models, arXiv preprint arXiv:2304.10592 (2023).
 - [145] H. Liu, C. Li, Q. Wu, Y. J. Lee, Visual instruction tuning, *Advances in neural information processing systems* 36 (2024).
 - [146] J. Achiam, S. Adler, S. Agarwal, L. Ahmad, I. Akkaya, F. L. Aleman, D. Almeida, J. Altenschmidt, S. Altman, S. Anadkat, et al., Gpt-4 technical report, arXiv preprint arXiv:2303.08774 (2023).
 - [147] W. Dai, J. Li, D. Li, A. M. H. Tiong, J. Zhao, W. Wang, B. Li, P. N. Fung, S. Hoi, Instructblip: Towards general-purpose vision-language models with instruction tuning, *Advances in Neural Information Processing Systems* 36 (2024).
 - [148] C. Zhou, C. C. Loy, B. Dai, Extract free dense labels from clip, in: *European Conference on Computer Vision*, Springer, 2022, pp. 696–712.